Pressure and concentration tuning of magnetic order in the heavy-fermion systems $CeNi_xPt_{1-x}$ and $CePd_{1-x}Ni_xAl$

Zur Erlangung des akademischen Grades eines
Doktors der Naturwissenschaften
an der Fakultät für Physik
der Universität Karlsruhe(TH)

genehmigte

Dissertation

von

Dipl.-Phys. Nadezda Bagrets

aus Gus-Chrystalny (Rußland)

Tag der mündlichen Prüfung: 24. Juli 2009

Referent: Prof. Dr. H. v. Löhneysen
Korreferent: Prof. Dr. E. Dormann

angefertigt am
Physikalischen Institut
Universität Karlsruhe (TH)

Juli 2009

Preface

This work is devoted to the experimental investigation of the rare-earth intermetallic compounds, $CeNi_xPt_{1-x}$ and $CePd_{1-x}Ni_xAl$, with a partially filled $4f$-shell. These systems belong to the class of so-called *heavy-fermion* compounds. Their characteristic feature is that the f-levels are positioned close to the Fermi energy, so that the ions of rare-earth metals can be found in different oxidation states, including the intermediate valence. Due to a hybridization of f-levels with conduction electrons, the density of states at the Fermi level is substantially increased, typically by 2 or even 3 orders in magnitude, compared to the ordinary metals. In other words, the electron effective mass m^* becomes much larger than that of a bare electron. This is one of the manifestations of the *Kondo effect*, when an exchange interaction between f-electrons and conduction ones ultimately leads to the singlet state formation. At low temperatures, the physical properties of metals, both the kinetic and the thermodynamic ones, are related to the nature of electronic states close to the Fermi level. Therefore, the radical change of the density of states substantially affects, for example, the specific heat coefficient $\gamma = C/T$, which can reach 1000 – 1500 $\mathrm{mJ/mol\,K^2}$ in heavy fermion compounds. To compare, in the ordinary metals γ is only of the order ~ 1 $\mathrm{mJ/mol\,K^2}$, and in the transition metals $\gamma \sim 10$ $\mathrm{mJ/mol\,K^2}$. Similarly, the magnetic susceptibility is rather large in rare-earth based materials.

Generally, the magnetic properties of the rare-earth systems derive from the partly filled f-orbitals, which behave like localized magnetic moments. In metals, the magnetic order is realized via the indirect, *RKKY exchange interaction* between localized f-ion spins.

On the other hand, the Kondo screening of local f-moments may prevent formation of magnetic order, thus competing with the RKKY interaction.

Some heavy fermion compounds can be tuned from a paramagnetic state through a phase transition into an ordered ferro- or antiferromagnetic state by changing pressure, composition of the compound or an external magnetic field. By the same means, the critical temperature of the phase transition can be altered for compounds already exhibiting the magnetic order. In a num-

ber of cases, the external parameters can drive the transition temperature to absolute zero, where the system undergoes a quantum phase transition. This transition is characterized by a change of the ground state of a many-body electron system due to its quantum fluctuations. In the parameter range close to the quantum critical point (QCP), nontrivial temperature dependences of physical quantities like specific heat, susceptibility, or resistivity, are usually observed. These temperature dependent variations of observables are different from those predicted by the Fermi-liquid theory. This has initiated substantial research over the past two decades: a variety of new phases and novel type of physics have been found.

We have investigated in this work the heavy-fermion $CeNi_xPt_{1-x}$ and $CePd_{1-x}Ni_xAl$ compounds with respect to their behaviour nearby the QCP which can be reached by chemical doping or chemical pressure. Low temperature magnetic properties of these materials are studied: they reveal unusual features, including dramatic screening of magnetic moments and spin-glass-like behaviour.

In Chapter 1, we give a theoretical introduction into the heavy-fermion compounds. The experimental methods used are described in Chapter 2. In Chapter 3, details about the sample preparation are presented. In Chapter 4, an overview on $CeNi_xPt_{1-x}$ system is given, where we discuss the previous investigations reported in the literature. In Chapter 5, magnetic measurements of doped $CeNi_xPt_{1-x}$ compounds under hydrostatic pressure are presented; a critical behaviour nearby a quantum phase transition is discussed. In Chapter 6, we present an overview on the antiferromagnetic CePdAl heavy-fermion system. The specific heat, AC-susceptibility, and magnetisation measurements on $CePd_{1-x}Ni_xAl$ are presented in Chapter 7.

Contents

Chapter 1

Introduction to $4f$-based intermetallic systems

1.1 Quasiparticles

A theoretical description of an interacting electron gas in a metal is a non-trivial problem due to a strong and long-range repulsive interaction between electrons. According to the phenomenological Fermi-liquid theory developed by Lev Landau in 1956, the low-lying excitations of the interacting electron system can be considered as a gas of noninteracting quasiparticles [1]. Namely, each many-particle excited state of the interacting fermions may be described by listing all occupied momentum $\mathbf{k}$ and spin σ quasiparticle states, just as in the non-interacting case. The quasiparticle energy $\varepsilon_{\mathbf{k}\sigma}$ is defined as the amount of energy by which the total energy increases when the particle is added to the system:

$$\varepsilon_{\mathbf{k}\sigma} = \frac{\delta E}{\delta n_{\mathbf{k}\sigma}},$$

where $\delta n_{\mathbf{k}\sigma}$ is the corresponding change in the distribution function $n_{\mathbf{k}\sigma}$. For the ground state ($T = 0$), $n_{\mathbf{k}\sigma}$ is just the Fermi distribution:

$$n_{\mathbf{k}\sigma}^{T=0} = \left.\frac{1}{1 + \exp[(\varepsilon_{\mathbf{k}\sigma} - \mu)/k_B T]}\right|_{T=0} = \theta(k_F - k),$$

where the Fermi momentum k_F is defined by the density of the quasiparticles: $n = k_F^3/3\pi^2$.

The quasiparticle concept is inherent to the mean field theory where each particle is considered to be moving in the potential collectively generated by all other particles. Quasiparticles carry the same spin, charge and momentum as the original electrons. However, a quasiparticle's effective mass m^*

(defined from the dispersion relation) can be quite different from that of a free electron. Since there remain some weak interactions between excitations, quasiparticles scatter off each other and acquire a finite lifetime. Thus, the whole concept is valid only if $k_B T \ll \mu \simeq \epsilon_F$, i.e. when $T \ll T_F$ [2]. This condition is satisfied for most of the metals in a whole range of temperatures when the systems are in the solid state.

1.2 Heavy fermion systems

The Fermi-liquid theory allows to describe a rather large class of systems, from simple metals like Cu to heavy-fermion systems with complicated and strong electronic interactions. The quasiparticle effective mass m^* determines the density of states per spin at the Fermi level [3]:

$$n(E_F) = \frac{m^* k_F}{2\pi^2 \hbar^2}.$$

In the case of simple metals, m^* takes values of several electronic masses, while for the so called heavy-fermion systems m^* can be sufficiently larger.

Heavy-fermion systems are compounds containing rare-earth or actinide elements. Variety of thermodynamic and transport properties of these systems reflects the multitude of localized states at the Fermi surface originating from atomic f-orbitals.

One of the characteristics of a heavy-fermion system is the electronic specific heat coefficient γ, which can be determined from the linear contribution to the specific heat: $C_{el} = \gamma T$. Here γ is proportional to the renormalized density of states [3] :

$$\gamma = \frac{2\pi^2 k_B^2}{3} n(E_F) = \frac{k_B^2}{3} \frac{m^* k_F}{\hbar^2},$$

and thus gives the information about the effective mass m^* of quasiparticles in a compound. For some heavy-fermion systems γ reaches values of several hundreds mJ/K^{2}mol (see, for instance, [4], [5], [6]). The large γ can be associated with a low energy scale $k_B T^*$ of the system via relation $n(E_F) \sim 3n/2E_F$ (with n being electron density) for the noninteracting electrons, and identifying $T_F = E_F/k_B$ with T^*.

Moreover, in systems with heavy fermions, at low temperatures the Pauli susceptibility χ depends only weakly on the temperature T [3, 8]. It is relatively large due to the enhanced effective mass m^* (see, for example [9]).

Another characteristic of a heavy-fermion system is the *Wilson ratio* [3, 11]:

$$R = \frac{\chi}{\gamma} \frac{\pi^2 k_B^2}{\mu_0 \mu_{\text{eff}}^2},$$

here μ_{eff} is a paramagnetic moment determined from the Curie-Weiss law at high temperatures. For ordinary metals this ratio is about $R \approx 1$, although for heavy-fermion systems it is $R = 2$–5 [3, 10].

The resistivity of heavy-fermion compounds is rather large at room temperature, typically of the order of 100 $\mu\Omega$cm [9]. At low temperatures, it can be fitted as:

$$\rho(T) = \rho_0 + AT^2,$$

where $\rho_{\text{ee}} = AT^2$ is a contribution due to electron-electron collisions, which is about six to seven orders of magnitude larger than the one observed in ordinary metals. Here ρ_0 is the residual resistivity arising from impurity scattering.

1.3 Intermediate valence

Among all heavy-fermion systems there is a class of rare-earth compounds for which the rare-earth ions are apparently in a state of an intermediate (non-integer) valence. Even pure Ce reveals the intermediate valence state after a volume collapse induced by external pressure [12], whereas in compounds such as SmB_6, $YbAl_2$, YbC_2, $CePd_3$, $CeSn_3$, and TmSe the intermediate valence is observed at ambient pressure (see [13] and references therein). All these systems have the common feature that there appears to be a mixture of rare-earth ions having either n or $(n-1)$ $4f$-electrons in a definite ratio (although in some cases this ratio varies substantially with temperature and pressure).

According to Jefferson *et al.* [13], appearance of the intermediate state in heavy-fermion systems can be understood as follows: applying a pressure lowers the Fermi energy (positioned close by a bottom of the conduction band) and reduces the excitation energy required to remove an f electron from an ion and to transfer it to the Fermi level. Interaction between f-electrons and conduction electrons causes rare-earth ions to fluctuate between $4f^n$ and $4f^{n-1}$ configurations resulting in a mixture of the corresponding valencies, the mean valence being intermediate between that of $4f^n$ and $4f^{n-1}$.

1.4 Single-impurity Anderson model

Already a system with isolated rare-earth magnetic ions embedded in a metallic matrix demonstrates a nontrivial physics known as a Kondo effect. Within a theoretical model developed by Anderson [14], a magnetic impurity is described by the f orbital of an incompletely filled inner atomic shell, hybridized with the conduction band [9]. The Hamiltonian can be written as (see, e.g., Hess *et al.* [9]):

$$H = \sum_{\sigma} E_f n_\sigma + \frac{1}{2} \sum_{\sigma} U_{ff} n_\sigma n_{-\sigma} + \sum_{k\sigma} \varepsilon_{\mathbf{k}} n_{\mathbf{k}\sigma} + H_{fd}, \tag{1.1}$$

where first two terms describe the f-electron subsystem, the third term describes the conduction electrons (hearafter, they are assumed to be d-like), and H_{fd} describes the coupling between these subsystems.

Consider f electrons: $n_\sigma = f^\dagger_\sigma f_\sigma$ represents the number of electrons in the f-orbital with a spin σ. $\sum_\sigma E_f n_\sigma$ represents the binding energy of a σ-spin electron in the f shell. The term involving U_{ff} describes the strong Coulomb repulsion between a pair of electrons occupying the f orbital. If a f-level lies below the Fermi energy ($E_f < E_F$), while $E_f + U_{ff} > E_F$, the impurity level is occupied mainly by a single electron and represents the local spin moment $S = 1/2$.

The noninteracting conduction electrons in band states are described by the kinetic energy term:

$$\sum_{k\sigma} \varepsilon_k n_{\mathbf{k}\sigma},$$

where $n_{\mathbf{k}\sigma} = d^\dagger_{\mathbf{k}\sigma} d_{\mathbf{k}\sigma}$ is the number of electrons with spin σ in the conduction band state labeled by the Bloch wave vector $\mathbf{k}$, $\varepsilon_{\mathbf{k}}$ is the dispersion relation of the conduction band.

The f- and d-electronic subsystems are coupled via spin conserving hybridisation term H_{fd}:

$$H_{fd} = \sum_{\mathbf{k}\sigma} \left[V^*_{\mathbf{k}} d^\dagger_{\mathbf{k}\sigma} f_\sigma + V_{\mathbf{k}} f^\dagger_\sigma d_{\mathbf{k}\sigma} \right].$$

It describes the processes whereby individual electrons can move out of the f level into the conduction band states, and the reverse process. The matrix element between the localized $|f\sigma\rangle$ state and the itinerant one $|d\,\mathbf{k}, \sigma\rangle$ is given by $V_{\mathbf{k}} = \langle f\sigma | H_{fd} | d\,\mathbf{k}, \sigma \rangle$.

Ordinary metals show a constant residual resistance, whereas the resistivity of Kondo systems shows a minimum, typical at low temperatures

($T < 20$ K), which originates from the conduction electrons scattering off the magnetic impurity described by H_{fd}. This experimentally observable minimum in resistivity is known as the *Kondo effect* [15]. Kondo has found, that the electrical resistivity shows a logarithmic dependence on temperature in the third order of the perturbation theory in exchange coupling $J = 2V^2\left[1/|E_f - E_F| + 1/(E_f + U_{ff} - E_F)\right]$ (see, for example, [3]):

$$\rho = \rho_B[1 + 2Jn(E_F)\ln(D/T) \ + \ \dots\ ],$$

where $\rho_B \propto J^2$, $n(E_F)$ is the local conduction-electron density of states per spin at the Fermi level, and D is the half-width of the conduction band. The perturbation theory for ρ breaks down at the Kondo temperature:

$$T_K = D\sqrt{Jn(E_F)}\exp\left[-1/Jn(E_F)\right].$$

Below T_K, the $S = 1/2$ impurity spin is fully compensated by a cloud of conduction electrons spins; an integral over a density of the screening cloud contains in total one electron spin, which is bound antiferromagnetically to the impurity.

In rare-earth compounds, e.g. with Ce atoms, orbital moments of f-ions are not quenched, so that in general the total impurity magnetic moment is composed of orbital and spin contributions. In addition, multiplet f-levels are split by the crystalline field, which gives rise to the anisotropic RKKY interaction. The picture of the Kondo effect becomes more complicated, but still a lowest temperature T_K can be defined in a theory, where the large impurity spin can be fully screened by conduction electrons; for further details, we refer to Ref. [16].

1.5 Anderson and Kondo lattice models

In a heavy-fermion system magnetic impurities occupy the lattice positions. The Anderson impurity model (1.1) should be generalized to the *periodic* Anderson model. In case of large U and negative E_f magnetic moments on the f sites are well-defined. Therefore, the Schrieffer-Wolff transformation can be applied, and the Hamiltonian of the resulting Kondo lattice model may be written in the form [3]:

$$H = \sum_{\mathbf{k}\sigma} \varepsilon_{\mathbf{k}} n_{\mathbf{k}\sigma} + J \sum_i \mathbf{S}_i \mathbf{s}_i,$$

with $J = 2V^2\left[1/|E_f - E_F| + 1/(E_f + U_{ff} - E_F)\right] > 0$. Direct exchange between f-electrons and direct hopping off are neglected in the Anderson and Kondo lattice models.

The Anderson model describes the Fermi liquid with two bands if the Coulomb interaction U_{ff} between two f-electrons, which can occupy one f-orbital with opposite spins (the second term in the single-impurity model), is small. At large U_{ff} limit, the Fermi-liquid state is formed below some coherence temperature T_{coh}. The local moments are screened by conduction electrons (generalization of the Kondo effect for the lattice). The Fermi volume below T_{coh} contains local moments and surrounding conduction electrons, and the resistivity follows the usual quadratic T dependence of the Fermi-liquid theory. For $T \gg T_{\mathrm{coh}}$ resistivity is rather small. The Fermi volume contains conduction electrons only, i.e. Kondo screening is absent. In the crossover region $T \sim T_{\mathrm{coh}}$ resistivity becomes very large due to incoherent Kondo scattering. This resistivity maximum is often used to define T_{coh}.

1.6 Quantum phase transitions and a non-Fermi-liquid behaviour

1.6.1 Doniach phase diagram

The screening of magnetic moments by conduction electrons in heavy-fermion systems competes with exchange interactions between the moments. The indirect RKKY interaction is provided by polarized conduction electrons and is given by (see [7]):

$$H_{\mathrm{RKKY}} = \sum_{i,j} I_{ij} \mathbf{S}_i \mathbf{S}_j,$$

with $I_{ij} = J^2 n(E_F) F(k_F R_{ij})$ and $F(x) = (x \cos x - \sin x)/x^4$. Here R_{ij} is the distance between lattice sites i and j; $n(E_F)$ is the conduction band density of states per spin at the Fermi level. The competition between the RKKY interaction and Kondo screening is represented in the well known Doniach diagram (figure 1.1).

For small coupling constant J, the RKKY interaction predominates over the Kondo singlet formation and the system can acquire magnetic order. Depending on the details of the electronic structure and the distance between the magnetic moments, ferromagnetic or antiferromagnetic order sets in. With increasing J, the Kondo screening becomes relevant and at large J the system remains paramagnetic.

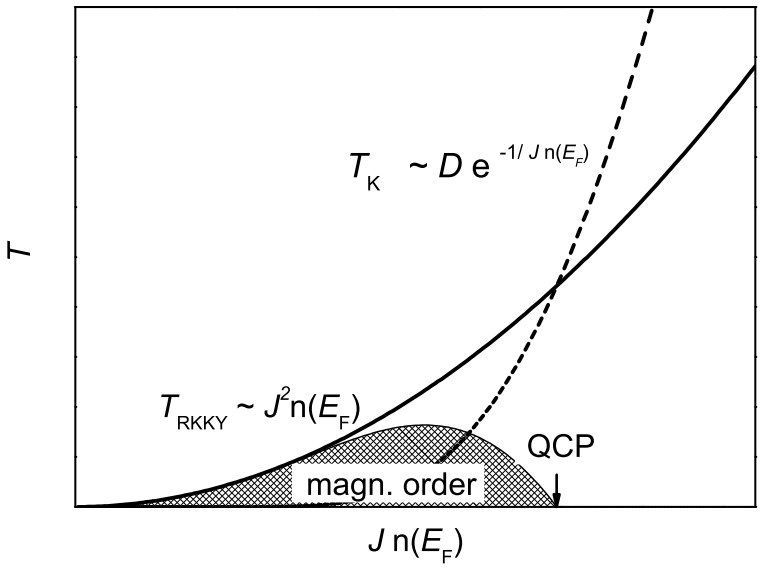

Figure 1.1: Phase diagram after Doniach [17]. For small J, the RKKY interaction dominates and magnetic order is possible. With increasing J, the Kondo screening becomes relevant, and at large J the system remains paramagnetic without magnetic order.

1.6.2 Quantum versus classical phase transitions

Inspecting the Doniach phase diagram (see Fig. 1.1), we observe a point $x_c = |J_c\, n(E_F)|$ where the energy scales of two competing interactions — Kondo screening ($k_B T_{\rm coh}$), and the RKKY exchange ($k_B T_{\rm RKKY}$) — become of equal value, so that the critical temperature T_c of the phase transition vanishes: $T_c \to 0$. Such a continious transition between different quantum phases of the system is called a quantum phase transition.

There is a conceptional difference between the classical phase transitions taking place at $T > 0$, and the quantum ones at $T = 0$. Classical phase transitions are driven by a competition between the energy of the system and the entropy of its thermal fluctuations. Classical transitions are characterized by the order-parameter (ϕ) fluctuations in space and time with the spacial correlation length ξ_r being divergent close by the transition.[1] At the same time, the characteristic frequency ω_ϕ of the order-parameter fluctuations tends to zero at $T \to T_c$, so that $\hbar\omega_\phi \ll k_B T_c$, and temporal fluctuations are of marginal importance.

[1] In the classical case, the correlation length ξ_r behaves as $\xi_r \sim t^{-\nu}$ when approaching the transition, where $t = |T - T_c|/T_c$, and $\nu > 0$ is a critical exponent.

In contrast, temporal fluctuations are not negligible for $T_c = 0$, but closely interwoven with spatial fluctuations. It turns out that the quantum system (with a spacial dimension d) behaves then like a fictitious classical system of dimension $(d + z)$, where z is referred to as the *dynamical exponent*. As some control physical parameter r (e.g., pressure p, magnetic field H, chemical composition x, etc.) is varied, quantum fluctuations can drive the system into a different phase, once r approaches a critical value r_c. The point $(r = r_c, T = 0)$ is called the quantum critical point (QCP). Quantum phase transitions take place, in particular, in the heavy-fermion compounds, where nontrivial temperature dependences of physical quantities like specific heat, susceptibility, resistivity, etc. are observed in the vicinity of the QCP: these nontrivial T-dependent variations of observables are different from those predicted by the Fermi-liquid theory [3, 8].

1.6.3 Renormalization group analysis

Quantum phase transitions in systems with itinerant electrons have been studied by Hertz [18] and Millis [19] using the renormalization group (RG) approach. Resulting phase diagram for the case $2 < d \leq z + 2$ (with z being dynamical exponent) is shown in Fig. 1.2.

Following Millis [19], we discuss four different regimes of the system's behaviour. The shaded area marks the ordered state, e.g. ferro- ($z = 3$) or antiferromagnetic ($z = 2$) one. Region I is the disordered quantum regime; here thermal effects are negligible. In this area the system behaves as a Fermi liquid. Region II is the perturbative classical regime. In this region the energy of quantum fluctuations is already lower than the thermal energy $k_B T$; however, the correlation length ξ of fluctuations is still determined by the distance $|r - r_c|$ from the QCP, similar to the quantum regime I. Regime III is the classical region, where the energy of quantum fluctuations is lower than the thermal energy $k_B T$. Here deviations from Fermi-liquid behaviour arise; the correlation length $\xi \propto T^{-\frac{z+1}{2z}}$ depends on temperature rather than on distance $|r - r_c|$ from the QCP. The solid line gives the dependence of the transition temperature T_c on $|r - r_c|$. Inside the dotted lines true three-dimensional classical critical phenomena occur. The theoretical predictions for thermodynamic and transport quantities, as well as the dependence of transition temperature (T_C or T_N) on the tuning parameter r are summarized in Table 1.1.

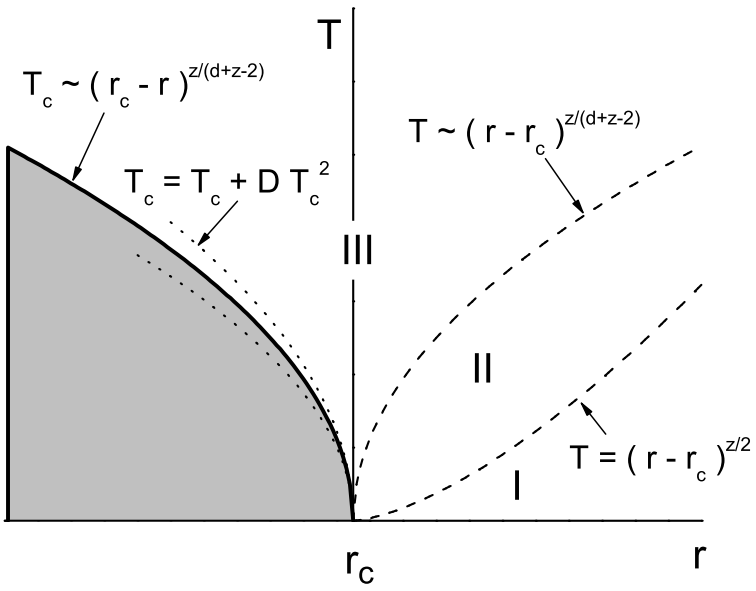

Figure 1.2: Phase diagram illustrating different regimes of a behaviour of the itinerant magnet for dimensions larger than two: $2 < d \leq z + 2$; after Millis [19].

	AFM, z=2 d=3	AFM, z=2 d=2	FM, z=3 d=3	FM, z=3 d=2
C/T	$\gamma - aT^{1/2}$	$c \log(T_0/T)$	$c \log(T_0/T)$	$T^{-1/3}$
$\Delta\chi$	$T^{3/2}$	$\chi_0 - dT$		
$\Delta\rho$	$T^{3/2}$	T	$T^{5/3}$	$T^{4/3}$
T_C/T_N	$(r_0 - r)^{3/2}$	$(r_0 - r)$	$(r_0 - r)^{3/4}$	$(r_0 - r)$

Table 1.1: Temperature dependencies from the spin fluctuation theories of Millis/Hertz reflecting a non-Fermi-liquid behaviour of itinerant magnets for the specific heat, susceptibility, and resistivity in the low temperature limit, plus the dependencies of the magnetic ordering temperature (T_C or T_N).

1.6.4 Local quantum critical point

The theories outlined above suggesting itinerant scenario to quantum phase transitions predict that the heavy Fermi-liquid (region I: $r > r_c$), incorporating both the conduction and f (or d) electrons, undergoes a transition to a spin-density wave metal when (at $T = 0$) r crosses r_c from the right. In this case, the local moments remain well screened by the Kondo effect during the transition [3]. In other words, the Fermi quasiparticles comprising the Fermi liquid in region I remain "intact" across the QCP.

In contrast, the theory for non-Fermi-liquid behaviour considered by Si *et al.* [21] and Coleman [22] is based on the assumption of local correlation phenomena in the QCP. In contrast to the itinerant scenario, Kondo screening breaks down at the QCP. In the ordered state ($r < r_c$), the f magnetic moments are supposed to be localized and they do not participate in the Fermi volume. However, above the magnetic transition ($r > r_c$) the moments are screened by conduction electrons and the Fermi volume includes both f magnetic moments and conduction electrons. Thus, the magnetic transition is associated with an abrupt reconstruction of the Fermi surface. Detailed discussion of these theoretical models are given in Ref. [3].

Chapter 2

Experimental methods

2.1 Crystal growth and structural characterisation

2.1.1 Crystal growth

Two different methods were used for the sample preparation: induction melting and arc melting.

Induction melting

For induction melting the initial materials are heated to their melting temperatures by means of eddy currents, which are produced by a high-frequency magnetic coil. Our radio-frequency (RF) generator is able to deliver a power up to 30 kW at a maximal frequency of 100 kHz. The RF-induction furnace allows working under ultra-high vacuum ($p \approx 10^{-10}$ mbar) or an argon atmosphere (for metals with a high vapor pressure). It is shown in Fig. 2.1. The quartz glass tube surrounds the cold water copper "finger" with molds for the starting materials. The tube can be evacuated with help of a ion-getter pump and can be eventually filled with purified argon. One of advantages of this method is the possibility to turn slowly the power up and down, controlling the temperature of the sample, for instance, with an optic pyrometer.

Arc melting

The arc furnace consists of a vacuum chamber, which can be evacuated down to 10^{-3} – 10^{-4} mbar and subsequently filled with an argon (Fig. 2.2). The starting materials are placed onto the water-cooled copper substrate, which serves as one of the two electrodes. The second electrode is the wolfram tip. A high voltage applied between the electrodes results in an electric arc. An arc has very high temperature (several thousand degrees) and the metals

Figure 2.1: RF-induction furnace.

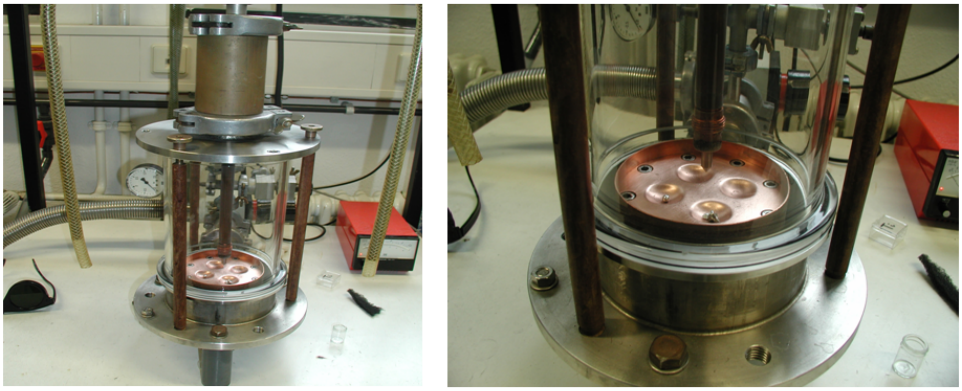

Figure 2.2: Arc furnace.

are melted and mixed in it. This method is convenient for metals with a high melting temperature (which may not be achievable by induction melting), but not for the elements with high vapor pressure (for instance Yb), because of possible high evaporation loss.

2.1.2 X-ray analysis

In order to determine the crystal structure X-ray measurements have been performed on powder samples; details of the experimental technique are given in Ref. [23]. The samples were powdered in an agate mortar and then attached on a the glass substrate with acetone. Measurements have been performed with a commercial Siemens D500 diffractometer. From the analysis of X-ray spectrum the lattice parameters have been calculated.

2.1.3 Atomic absorption spectroscopy

Atomic absorption (AA) spectroscopy uses the absorption of light to measure the concentration of gas-phase atoms. Since samples are solids, they have been solved in HNO_3/H_2O in 1:3 proportion with a small amount of HCl (0.5 ml) under continuous heating. The solution has been pulverized together with burning gas and transport gas in a mixing chamber. The cathode ray tube produces light with a noticeable wave length (232.0 nm for Ni and 247.6 nm for Pd). It is absorbed by metal atoms from the sample. The analyte concentration is determined from the degree of absorption.

2.2 Low-temperature measurements

2.2.1 Cryostats

For the experiments, three different cryostats were used, depending on the temperature range : a standart ^{4}He bath cryostat (1.3 K<T<300 K), a ^{3}He cryostat (0.3 K<T<4.2 K), and ^{3}He/^{4}He dilution refrigerator (50 mK<T<2.5 K). All cryostats are equipped with superconducting magnets to allow measurements in fields up to 20 T.

2.2.2 Measurements methods

AC susceptibility

The magnetic AC susceptibility characterizes the response of the magnetic material on the applied AC field:

$$\chi_{AC} = dM/dH$$

which can be measured by means of a susceptometer. The susceptometer consists of a pick-up coil surrounding a sample and a field coil. The field coil

is the source of the time-dependent magnetic field. The induced voltage in the pick-up coil is proportional to the magnetic flux:

$$V = \omega N A \mu_0 B(\chi_{\text{sample}} f + \text{background})$$

where N is the winding number of the pick-up coil, A its cross-section, f is the volume filling factor, B is magnetic field from the field coil, and ω is the AC frequency.

The coil body was made of nonmagnetic Araldit. The field coil has 755 turns of 60 μm copper thick wire. Two pick-up coils were made of 50 μm copper thick wire. They were wound in opposite directions relative to each other in order to reduce the background. Each pick-up coil consisted of 598 turns. When winding the coils, particular care was taken to ensure a perfect arrangement of the individual turns. A temperature sensor was mounted close to the susceptometer on the sample holder. The susceptometer is small enough, that one can neglect the temperature gradient inside.

Magnetisation measurements

The magnetisation measurements were performed using a vibrating sample magnetometer (VSM) with a superconducting magnet from Oxford Instruments, with fields up to 12 T. Its operating temperature range is 1.5 – 300 K. The samples are top loaded on a sample rod and detachable tips are supplied to allow a range of different shapes to be attached with vacuum grease or Teflon tape. The tips are made of a thermal plastic in order to reduce their background signal.

The measuring method of the VSM is due to Foner [25]. The sample is attached to the lower end of the tip made to oscillate vertically, typically over 0.1 – 1.5 mm with frequencies between 40 – 80 Hz. If the sample is magnetized (either spontaneously or in response to an external applied field) the oscillation will induce an AC signal in a set of suitably placed pick-up coils. The amplitude of the signal is proportional to the magnetic moment of the sample. The pick-up coils are connected as a gradient pair such that the induced voltages in each coil add. A lock-in amplifier is tuned to the vibration frequency using a reference signal from the vibration controller and detects the in-phase voltage from the pick-up coils.

The DC susceptibility is defined by:

$$\chi_{DC} = \frac{\delta M}{\delta H}$$

This can be approximated by $\chi_{DC} \approx \frac{M}{H}$ for small H. M is the magnetic moment per unit formula, H is the internal field. In the case of magnetisation measurements under pressure, field sweeps and temperature sweeps

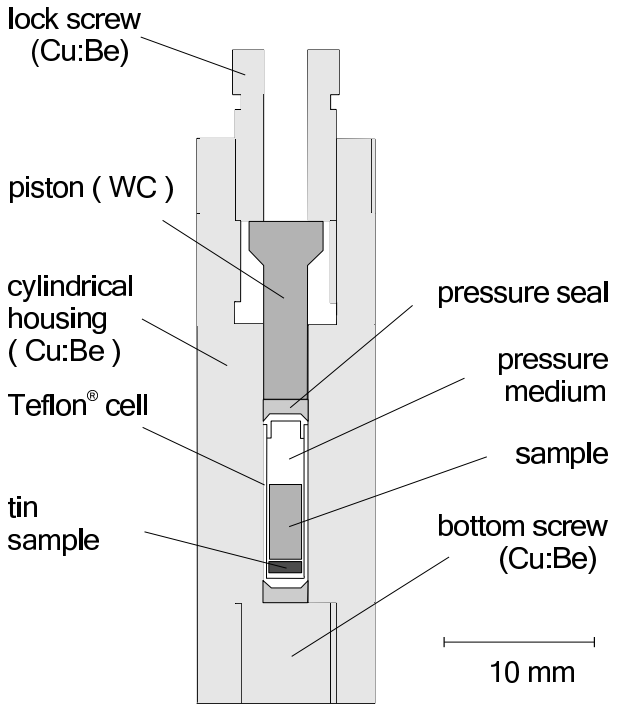

Figure 2.3: Schematic of the clamp type pressure cell. The outer diameter of the cell is 11.7 mm, bore diameter is 3 mm. The total length of the cell is 32.7 mm. The total lenght of the Teflon cell is 8 mm, its wall thickness is approximately 0.2 mm.

were recorded for the pressure cell with and without the sample in order to be able to substract cell contribution from the raw data. The demagnetisation correction was estimated to be about 1% of magnetisation.

Measurements under hydrostatic pressure

A CuBe clamp pressure cell with a bore diameter of 3 mm was used for measurements under pressure (see Fig. 2.3 for further details). After the CuBe-parts were prepared, they were sealed in a quartz tube and annealed at 315 °C for two hours. The pressure cell was autofrettaged before usage in order to get rid of permanent deformations.

The sample and a piece of tin were enclosed into a teflon cell filled with an ethanol-methanol mixture, which was used as a pressure medium. The cell was pressurized at room temperature with the help of maraging steel pushrod and the pressure was "clamped in" by lock screw. Each teflon cell was used only once.

For the cell used, the highest attainable pressure was 13 kbar. High pres-

sure values could be only reproduced when a new piston was used. The pressure value was determined by measuring the Sn superconducting transition temperature T_c^{Sn} (which depends on the pressure). Measurements of T_c^{Sn} were carried out at a cooling rate of 0.5 K/min using the vibrating sample magnetometer (VSM).

Specific heat measurements: Quasi-adiabatic heat-pulse method

The specific heat was measured with a semi-adiabatic heat pulse technique. This method consists of measuring the variation of the sample temperature ΔT after the heat pulse ΔQ, whereas sample and environment temperatures during the measurements are quasi-statically balanced. The energy supplied to the sample due to electric pulse is $\Delta Q = IV\Delta t$. After the heat pulse, the time dependence of the sample temperature follows an exponential decay law which can be fitted with a single decay constant. The molar heat capacity is defined by

$$C_p(T) \approx \frac{1}{n}\frac{\Delta Q}{\Delta T}$$

where n is the number of moles and $T = T_1 + \Delta T/2$. The sample was glued between a temperature sensor and a heater with a small amount of vacuum grease, and was supported by a nylon wire string inside the sample holder. It was controlled that the sample, the sensor and the heater were well thermally coupled, whereas the nylon wire was nearly non-heat conducting.

To measure the temperature of the samples carbon thermometer was used. It was calibrated using capacitance thermometer, which was anchored with the temperature scale of the superconducting fixed point device. The lowest measured temperature is of 10 mK. The heater was made from a PtW-alloy wire.

Chapter 3

Sample preparation and characterisation

Two different methods for the samples preparation were used: arc melting and induction melting.

3.1 Sample preparation

The polycrystalline samples of $CeNi_xPt_{1-x}$ were prepared using both arc and induction melting techniques. The purity of the starting materials was Ce 99.9, Ni 99.95, Pt 99.999. Using the induction melting we were able to produce samples of larger size. No qualitative difference between the samples prepared by the two different methods was observed.

In many cases sufficient structural order is not achievable by induction melting or arc melting. To improve the quality, each of $CeNi_xPt_{1-x}$ samples were annealed. The samples were inserted in an evacuated quartz tube and placed into the annealing oven for several days. The samples with small Pt content have been annealed at 500°C, the CePt sample was annealed at 750°C. Weight losses due to evaporation were below 0.5% and after annealing were below 0.1%.

The polycrystalline $CePd_{1-x}Ni_xAl$ samples were prepared by arc-melting of the pure Ce, Pd, Ni, Al (purity Ce 99.9, Ni 99.95, Pd 99.95 and 99.998, Al 99.999.) elements in their stoichiometric ratio using an argon atmosphere under titanium gettering. To achieve a good homogeneity, the samples were turned over and remelted several times. The weight loss after the melting did not exceed 0.5%. All $CePd_{1-x}Ni_xAl$ samples crystallize in the hexagonal ZrNiAl-type structure and have been used as-cast since annealing causes a change in their structure.

3.2 Characterisation of $CeNi_xPt_{1-x}$ samples

The X-ray diffraction results are shown in Fig. 3.1 for a CePt polycrystalline sample, and in Fig. 3.2 for the series $CeNi_xPt_{1-x}$. The CrB orthorhombic structure type is confirmed for all samples. The lattice constants of $CeNi_xPt_{1-x}$ are summarized in Table 3.1.

In the diffractogram of CePt we have observed additional peaks, which are labeled with an "x". They can be ascribed to a small amount Ce_3Pt_4, which orders antiferromagnetically below 2.8 K [26]. However, when magnetisation measurements on CePt sample have been performed, no any additional magnetic transitions have been found down to 2.5 K, except for those related to the CePt compound.

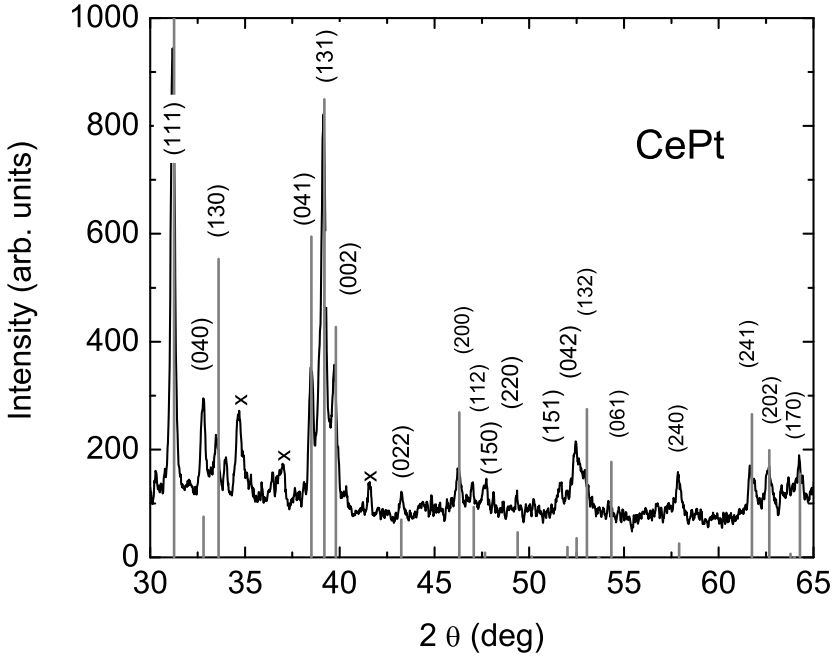

Figure 3.1: X-ray diffraction pattern for CePt compound. Gray lines indicate expected Bragg peak positions.

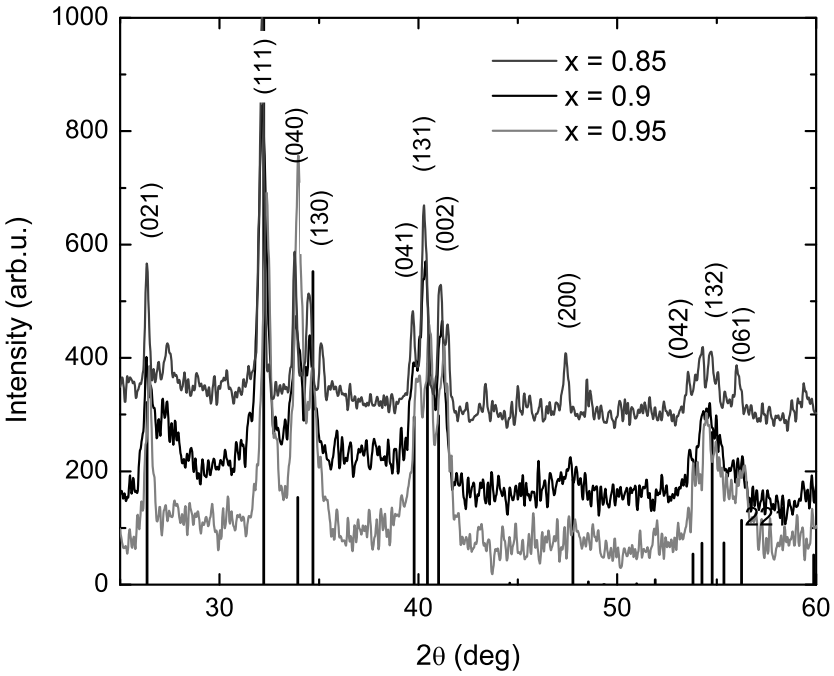

Figure 3.2: X-ray diffraction patterns for $CeNi_xPt_{1-x}$ polycrystalline samples.

$CeNi_xPt_{1-x}$	a (Å)	b (Å)	c (Å)
$CeNi_{0.95}Pt_{0.05}$	3.7858	10.5488	4.3740
$CeNi_{0.9}Pt_{0.1}$	3.8223	10.5780	4.3800
$CeNi_{0.85}Pt_{0.15}$	3.8303	10.6376	4.3868

Table 3.1: Lattice parameters of $CeNi_xPt_{1-x}$.

3.3 Characterisation of $CePd_{1-x}Ni_xAl$ samples

X-ray diffraction measurements and atom absorption spectroscopy (AAS) measurements were performed for all $CePd_{1-x}Ni_xAl$ samples. AAS results are shown in Table 1. AAS allows to determine the masses of Ni and Pd in the $CePd_{1-x}Ni_xAl$ sample with known mass. The mass of Ce was calculated with:

$$m_{Ce} = \frac{m_S - m_{Ni} - m_{Pd}}{1 + \frac{M_{Al}}{M_{Ce}}},$$

where m_S is the sample mass, m_{Ni} and m_{Pd} are masses of Ni and Pd, that were determined by AAS, M_{Al} and M_{Ce} are molar masses of Al and Ce, respectively. The Ni and Pd contents are given by:

$$x = \frac{m_{Ni}}{m_{Ce}\frac{M_{Ni}}{M_{Ce}}} \quad \text{and} \quad 1 - x = \frac{m_{Pd}}{m_{Ce}\frac{M_{Pd}}{M_{Ce}}},$$

where x and $1 - x$ are Ni and Pd contents, respectively.

A LuPdAl sample was also prepared and analyzed. It serves as reference compound for specific heat measurements. The La-based compound (LaPdAl in this case), which might be the first thought to be used as a nonmagnetic reference system for Ce compounds has a different crystallographic structure.

X-ray diffraction measurements show the single-phase ZrNiAl hexagonal structure for CePdAl (Fig. 3.3), LuPdAl (Fig. 3.4), and for all $CePd_{1-x}Ni_xAl$ samples (Fig. 3.5). The corresponding lattice constants are presented in Table 3.3. These data suggest that Ni doping induces a chemical pressure — the lattice constants are reduced with increasing of Ni content, whereas a ratio a/c remains approximately constant. The lattice parameters have been determined for the samples with x=0.05 and x=0.1 only, since at such low Ni concentrations shifts of X-ray peaks relative to each other are too small.

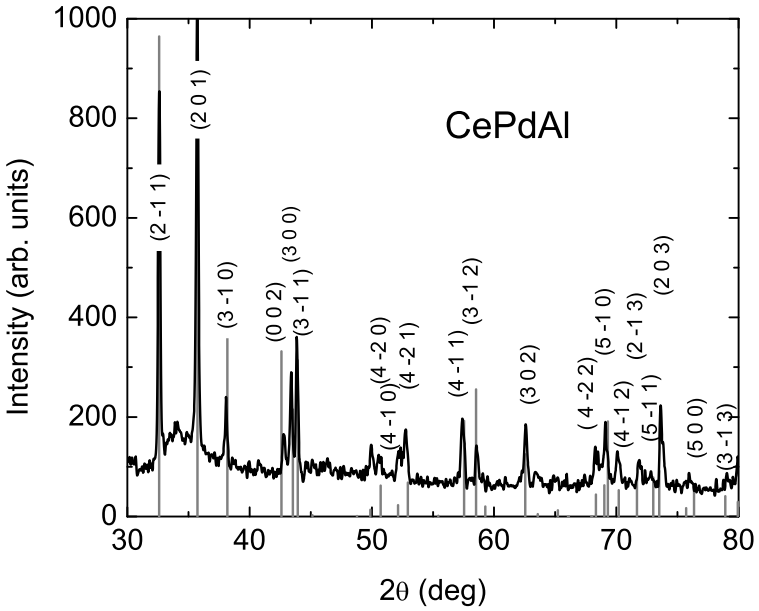

Figure 3.3: X Ray-diffraction pattern for CePdAl.

$CePd_{1-x}Ni_xAl$	Ni content (per mol alloy)	Pd content (per mol alloy)	Ni+Pd content (per mol alloy)
$CePd_{0.98}Ni_{0.02}Al$	0.020	0.970	0.99
$CePd_{0.96}Ni_{0.04}Al$	0.039	0.963	1.00
$CePd_{0.95}Ni_{0.05}Al$	0.049	0.899	0.95
$CePd_{0.94}Ni_{0.06}Al$	0.067	0.984	1.05
$CePd_{0.92}Ni_{0.08}Al$	0.083	0.988	1.07
$CePd_{0.90}Ni_{0.10}Al$	0.102	0.885	0.90
$CePd_{0.87}Ni_{0.13}Al$	0.131	0.915	1.05

Table 3.2: AAS measurements for $CePd_{1-x}Ni_xAl$ system. First column: nominal Ni content x and Pd content $1-x$, second and third columns: Ni and Pd contents were determined by AAS independently.

$CePd_{1-x}Ni_xAl$	a (Å)	c (Å)	a/c
CePdAl	7.2219	4.2218	1.710
$CePd_{0.95}Ni_{0.05}Al$	7.2019	4.2180	1.707
$CePd_{0.9}Ni_{0.1}Al$	7.1887	4.2058	1.709

Table 3.3: Lattice parameters of $CePd_{1-x}Ni_xAl$ compounds.

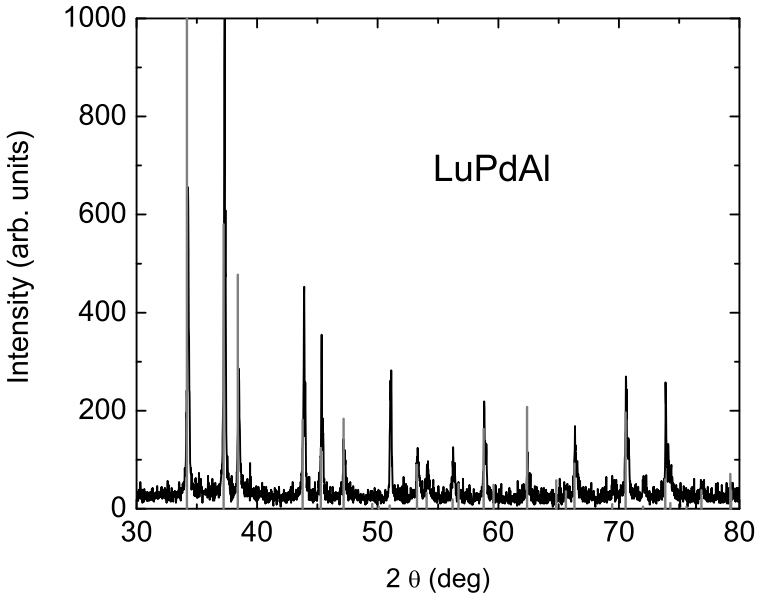

Figure 3.4: X-ray diffraction pattern for LuPdAl.

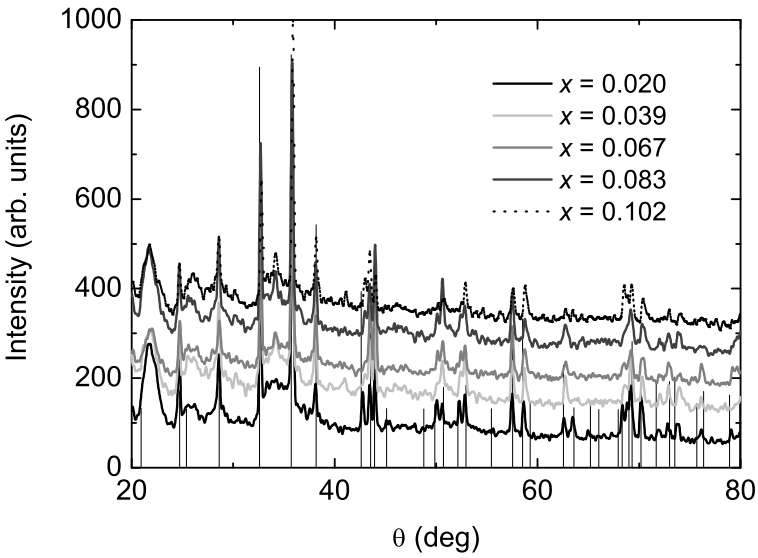

Figure 3.5: X-ray diffraction patterns for $CePd_{1-x}Ni_xAl$ policrystalline samples.

Chapter 4

Magnetic properties of CeNi, CePt, and their pseudobinary alloys $CeNi_xPt_{1-x}$

In Ce-based compounds with transition metals having an almost filled d-band the electronegativity mismatch between constituents enforces the Fermi level to be placed differently compared to $4f$ Ce levels depending on the stoichiometry. Therefore, a variety of Ce states are expected: a stable magnetic 3+ state (corresponding to a [Xe].$4f^1$ atomic configuration), a 3+ state hybridized with the conduction electrons leading to the Kondo screening, an intermediate valence state, and a non-magnetic 4+ state [27]. In particular, interest in Ce-Pt and Ce-Ni alloys has been attracted over the years, since different electronic states indeed have been observed: their manifestation in magnetic and transport properties can be studied in detail.

In this chapter, we present a short overview over the structural and magnetic properties of Ce-Pt and Ce-Ni compounds. While in Ce-Pt systems, the Ce ions are found in 3+ magnetic state [27], partially compensated by Kondo screening [28], CeNi is an intermediate valence compound [29] (where the Fermi energy is positioned much closer to the $4f$ levels than in CePt) which behaves like an enhanced Pauli paramagnet exhibiting strong charge and spin fluctuations. We further discuss the interplay between the RKKY interaction and Kondo screening in $CeNi_xPt_{1-x}$ compounds [30, 31]. This competition is described by Doniach phase diagram (see Chapter 1), where a parameter $|Jn(E_F)|$ controls the characteristic energies of two interactions: $k_BT_{RKKY} \propto |Jn(E_F)|^2$, and $k_BT_K \propto \exp(-1/|Jn(E_F)|)$. Here $n(E_F)$ is the density of states at the Fermi level, whereas $J \propto |V|^2/(E_0 - E_F)$ measures the exchange coupling strength between localized spins: it depends on the hybridization V between the f-electrons and conduction electrons, as well

as on the offset of the Fermi energy with respect to the position E_0 of the $4f$ Ce levels. By alloying CePt with Ni allows one to alter the difference $|E_F - E_0|$. This opens a way to explore the whole range of relative strengths of interactions, and study the progressive variation of the Ce^{3+} state towards the intermediate valence in an isostructural system.

4.1 The binary compounds Ce-Pt

The phase diagram of Ce-Pt exhibits a large number of well-defined compounds, which crystallize in the orthorhombic CrB type of structure. The Fermi energy of pure Pt is close to that of Ce and is placed above the $4f$ level (Fig. 4.1) [27]. This is reflected in magnetic properties which indicate that in all Ce-Pt compounds the Fermi level alignment depends rather weakly on the stoichiometry (Fig. 4.1).

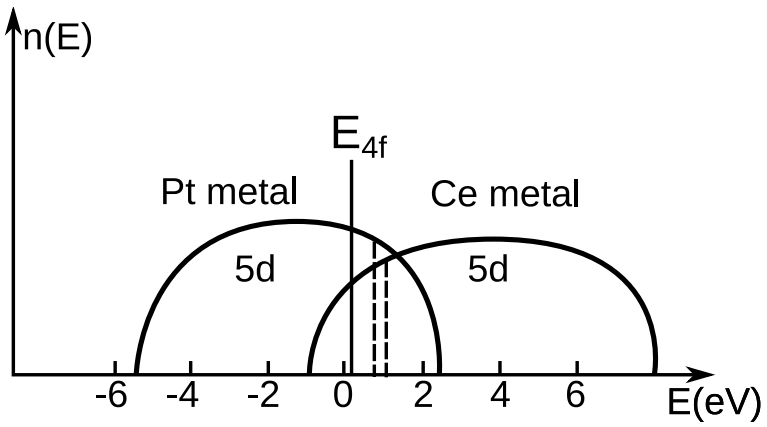

Figure 4.1: Schematic representation of the density of states $n(E)$ of pure platinum and cerium [27]. Dashed lines correspond to Fermi levels of Ce and Pt.

In all Ce-Pt compounds, Ce is trivalent [27]: no anomaly of lattice parameters is observed; above 20 K the susceptibility follows the Curie-Weiss law with effective moments corresponding to the Ce^{3+} free-ion value. The magnetic interactions between Ce atoms are of the RKKY type and can lead to a magnetic order. $CePt_3$ is paramagnetic down to 4.2 K [32, 33]. $CePt_5$ and $CePt_2$ orders antiferromagnetically below $T_N \simeq 1$ K [34] and $T_N = 1.7$ K [35], respectively. On the other hand, CePt and Ce_7Pt_3 order ferromagnetically at 5.8 K and 7 K, respectively [28], [36]. However, in CePt a reduction of the spontaneous magnetization, a low value of the magnetic entropy at

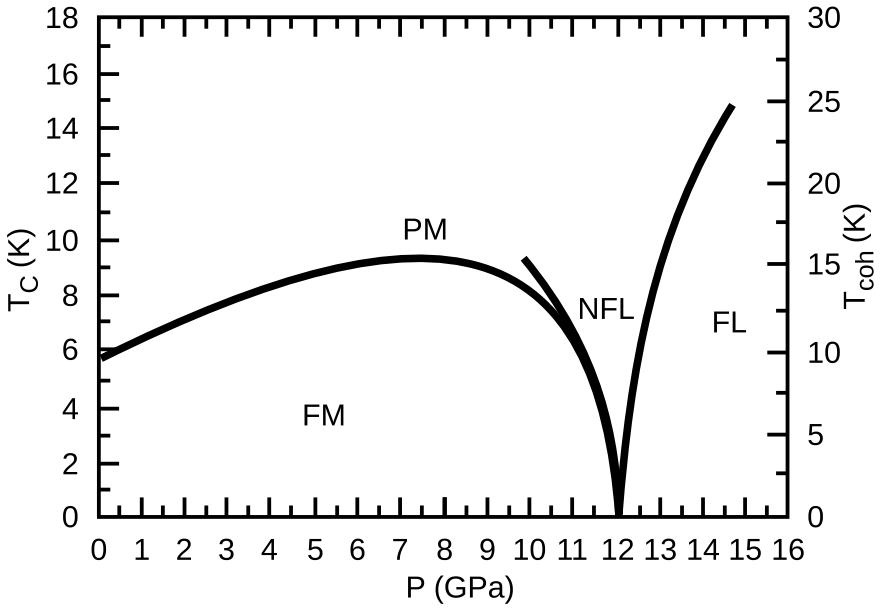

Figure 4.2: Temperature-pressure ($T - p$) phase diagram for CePt (after Larrea *et al.* [37]).

T_C, and a decrease of the magnetic resistivity at high temperatures suggest the existence of the Kondo effect [28].

The effect of external pressure p on the CePt compound was thoroughly studied by Larrea *et al.* [37]. Their phase diagram is presented in figure 4.2. Susceptibility measurements have shown that for $p \lesssim 12$ GPa the ferromagnetic order remains, while the magnitude of the ordered Ce moments decreases under high applied pressure. T_C first rises with p, approaches a maximum at 7 GPa, and then drops down to $T_C \to 0$. The initial pressure coefficient $d\ln T_C/dp$ was found to be $\simeq 0.115$ GPa^{-1}. This value is somewhat smaller than that reported by Itoh *et al.* [38]. For pressures $p \gtrsim 12$ GPa, no signature of ordered magnetic states in the AC-susceptibility signal could be detected. For the temperature dependence of the resistivity at $p \approx 12.2$ GPa, a power-law behaviour $R(T) \sim T^n$ was reported with an effective exponent $n = 2$ in the nonmagnetic Fermi-liquid regime (below $T_{\rm coh}$), and $n = 1.34$ in the non-Fermi-liquid critical regime (above $T_{\rm coh}$). Altogether, the reported data [37] gave strong evidence for the existence of a quantum critical point (QCP) at $p_c \simeq 12.1$ GPa. The authors estimated the shift exponent ψ describing the pressure dependence of $T_C(p)$ close to p_c, $T_C \propto |\delta|^\psi$, in terms of distance $\delta = |p - p_c|$ to the QCP. The best fit for the exponent ψ was the mean-field value ψ=1/2.

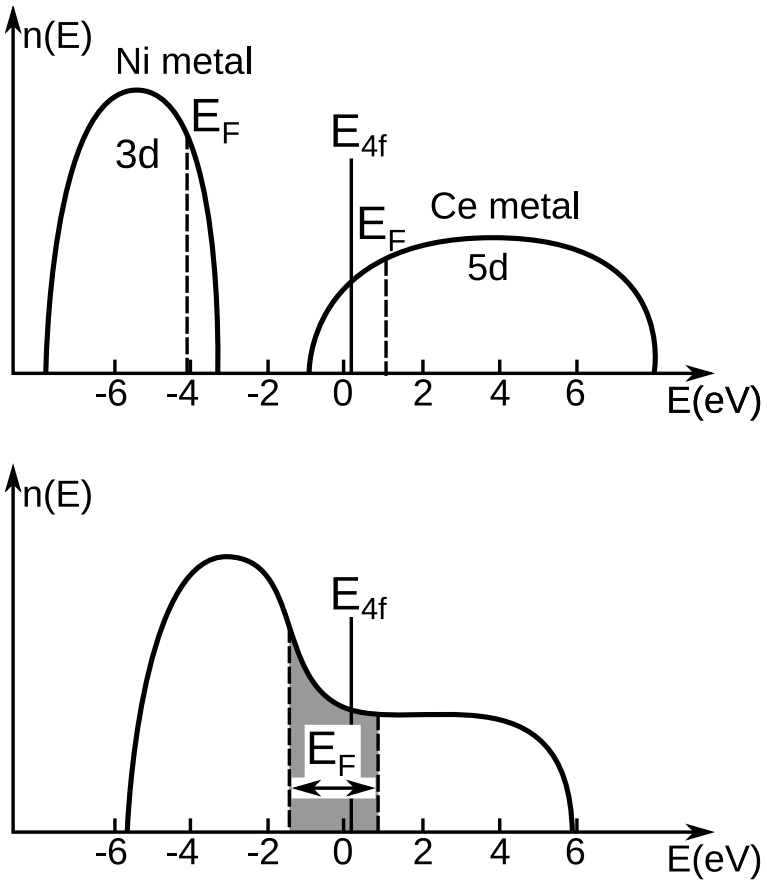

Figure 4.3: Schematic representation of the density of states $n(E)$ of (a) pure Ni and Ce, and (b) Ce-Ni compounds (after [27]).

4.2 The binary compounds Ce-Ni

Alloying Ce with Ni allows one to study not only the $4f$ instability but also the onset of $3d$ magnetism. The phase diagram in this case exhibits a large number of well-defined Ce-Ni compounds with various compositions. The band structure of Ce-Ni results from the overlap of the narrow Ni $3d$ band with the wider Ce $5d$ band of higher energy (Fig. 4.3) [27]. The $5d$ electrons of Ce are partially transferred to the $3d$ band. The two bands are merged together and hybridized states are formed at the top of the $3d$ band and at the bottom of the $5d$ band. With increasing Ni content, the Fermi level shifts downwards in energy with respect to the $4f$ level. $CeNi_5$ and Ce_7Ni_3 represent the extreme cases with the largest and the least possible amount of Ni. The Fermi energy thus takes the lowest and the highest values in case

of $CeNi_5$ and Ce_7Ni_3, respectively.

We discuss the properties of CePt in more detail. The lattice parameter analysis and studies of thermal expansion show that CeNi is an intermediate valent compound where the valency of Ce varies from 3.5 to 3.3 between 4 K and 300 K [29]. It behaves like an enhanced Pauli paramagnet where the magnetic susceptibility passes through a maximum at $\sim$ 140 K. The origin of magnetism in CeNi was studied by polarized neutron diffraction experiments [29]. While in $CeNi_5$ the magnetic order originates from the Ni $3d$ states [39], the induced magnetization in CeNi arises from the $4f$ electrons of cerium. No magnetic density was found on Ni sites.

4.3 The series $CeNi_xPt_{1-x}$

The $CeNi_xPt_{1-x}$ pseudobinary alloys are of particular interest. They all crystallize in the same orthorhombic CrB-type structure. In the limiting cases, $x = 1.0$ or $x = 0$, cerium is found in two almost extreme states, intermediate valence and magnetic Ce^{3+}. For a pseudobinary alloy, $CeNi_xPt_{1-x}$, the progressive variation of the Fermi level E_F as function of x may lead to a continuous change of the oxidation state of Ce ions. In addition, a substitution of Pt by Ni produces a chemical pressure effect (due to a smaller size of Ni atoms compared to Pt) and thus may cause a change in the electronic properties. Summarizing, in the intermetallic alloys $CeNi_xPt_{1-x}$ one expects to observe the following sequence with increasing x [31]: ferromagnetic order $\rightarrow$ trivalent spin-fluctuation behaviour (Kondo effect) $\rightarrow$ intermediate valence state.

The Curie temperature T_C and the Kondo temperature T_K of the series $CeNi_xPt_{1-x}$ compounds as function of the Ni content x are shown in Fig. 4.4, as reported by Gignoux and Gomez-Sal [31]. T_C was obtained from Arrott plots. The similarity of Fig. 4.4 and the Doniach diagram is evident. The RKKY interaction dominates for $x \leq 0.9$, where the system orders ferromagnetically. Magnetisation measurements of samples with $x \geq 0.95$ have shown that these compounds are nonmagnetic [31]. Moreover, the form of the T_C curve is essentially similar to the one obtained from pressure measurements (cf. Fig. 4.2): T_C first goes up with increasing Ni content, approaches a maximum at $x \sim 0.6$, and finally drops down for large values of x [27].

As argued by Gignoux and Gomez-Sal [31], the variation of T_C as a function of the Ni content is in qualitative agreement with that calculated as a function of the product $|Jn(E_F)|$ in the Doniach model. Here J is the coupling constant between the $4f$ shell and the conduction band, $J = 2|V|^2/(E_0 - E_F)$, where V is a hopping matrix element between f and con-

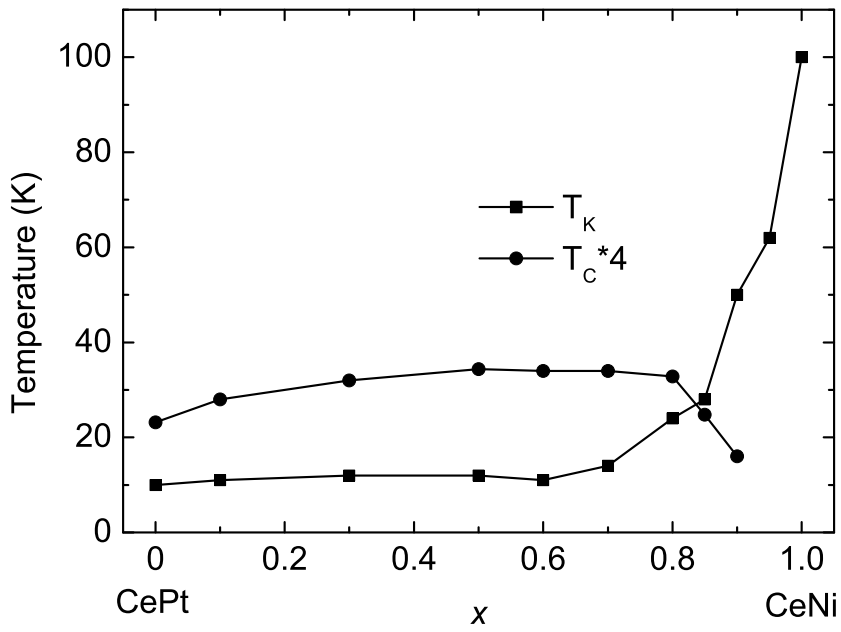

Figure 4.4: The Curie temperature T_C, and the Kondo temperature T_K of $CeNi_xPt_{1-x}$ compounds as function of the Ni content x (after Ref.[31]).

duction electrons, E_0 is the $4f$ level, and E_F is the Fermi level. The main contribution to the increase of $|Jn(E_F)|$ with increasing Ni content arises from the decrease of $|E_0 - E_F|$. As mentioned above, in Pt the Fermi level lies above the Fermi level of Ce metal (cf. Fig. 4.1), whereas in Ni it lies below (cf. Fig. 4.3). Therefore, CePt is characterised by a small parameter $|Jn(E_F)|$, so that the exchange interactions overcome the Kondo effect which remains weak. In contrast, Ce is found in the intermediate valence state in CeNi: there E_F is placed closer to the $4f$ level E_0, and $|Jn(E_F)|$ is large. Substituting Pt by Ni in CePt, the Fermi level approaches the $4f$ level, leading to an increase of the product $|Jn(E_F)|$.

Gignoux and Gomez-Sal [31] determined the lattice parameters of polycrystalline samples of $CeNi_xPt_{1-x}$ and $LaNi_xPt_{1-x}$. The cell volume is plotted in Fig. 4.5 as function of the Ni content x. For $x < 0.8$ the change of lattice parameters of $CeNi_xPt_{1-x}$ follows the same moderate variation as for $LaNi_xPt_{1-x}$ (see Fig. 4.5). However, for $x \geq 0.8$ the cell volume of $CeNi_xPt_{1-x}$ drops with a larger slope. This enhanced slope was attributed by authors of Ref. [31] to the Ce state changing from a trivalent state to an intermediate valence, which is associated with a shrinking of the Ce ionic radius.

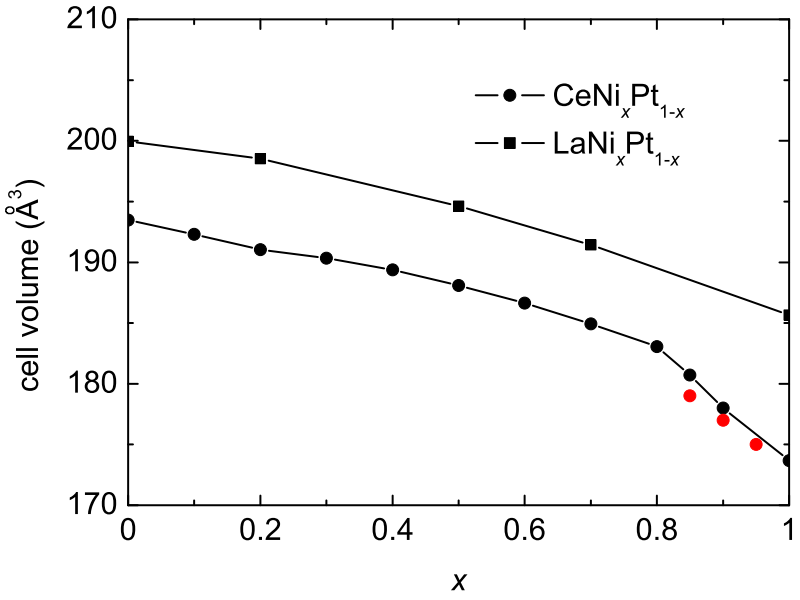

Figure 4.5: The cell volume of $CeNi_xPt_{1-x}$ and $LaNi_xPt_{1-x}$ compounds as function of Ni content x (after [31]). Red points correspond to our data.

In the later work by Espeso *et al.* [30] X-ray absorption spectroscopy studies have been performed on $CeNi_xPt_{1-x}$ to clarify whether the observed transition to a nonmagnetic state corresponds to a change of Ce valence or is due to a competition between the RKKY exchange interaction and the Kondo effect. Results of this investigation have shown that the behavior of $CeNi_xPt_{1-x}$ is in agreement with the Doniach diagram for $x \leq 0.9$. Therefore, it has been argued [30] that a transition into a nonmagnetic state is due to progressive screening of the $4f$ shell as the result of the competition between RKKY exchange interaction and the Kondo effect, but is *not* due to the change of the Ce valence. According to Gignoux and Gomez-Sal [31], at the instability point, $x \simeq 0.9$, the system is characterized by a reduced critical temperature T_C= 4.0 K (cf. $T_C = 5.8$ K for CePt) and a very small, almost screened low-temperature magnetic moment $M = 0.047\mu_B$ of the Ce ions. Therefore, external pressure applied to the $CeNi_xPt_{1-x}$ alloy, which is already close to the magnetic instability, could push the system further along the Doniach diagram towards a quantum critical point: a thorough discussion of this topic is presented in the following Chapter 5.

Chapter 5

Pressure effects in $CeNi_xPt_{1-x}$

In this chapter we present the results of magnetic measurements on $CeNi_xPt_{1-x}$ under pressure, with Ni content $x = 0.85$ and 0.9. These systems are close to the instability point, where magnetic moments are very sensitive to the lattice volume. Therefore, a "moderate" external pressure ($\sim$ 1 GPa) can tune the system to a quantum critical point (QCP) as we demonstrate by our measurements. In contrast, very high external pressure ($\sim$ 12 GPa) is required to reach the QCP in the case of CePt [37]. We compare the effect of doping (*chemical pressure*) with external hydrostatic pressure: our results together with the literature data are summarized in a "pressure-and-doping" diagram for $CeNi_xPt_{1-x}$ compounds.

5.1 $CeNi_xPt_{1-x}$: magnetisation measurements

In this section, the magnetisation measurements on $CeNi_xPt_{1-x}$ are presented. The measurements were carried out with a vibrating sample magnetometer (VSM, see Chapter 2). From the low field magnetisation (M) data the DC-susceptibility is approximately given by $\chi_{\rm DC} \approx M/H$, where H ($\sim$ 1000 Oe) is the magnetic field. The temperature dependent susceptibili-

$CeNi_xPt_{1-x}$	$\mu_{\rm eff}$ (μ_B)	T_C (K)	θ_p (K)
$CeNi_{0.9}Pt_{0.1}$	2.43	4	-100
$CeNi_{0.85}Pt_{0.15}$	2.56	6.2	-87
CePt	2.58	6	-7

Table 5.1: Effective paramagnetic moments $\mu_{\rm eff}$, Curie temperatures T_C, and paramagnetic Curie-Weiss temperatures θ_p for $CeNi_xPt_{1-x}$

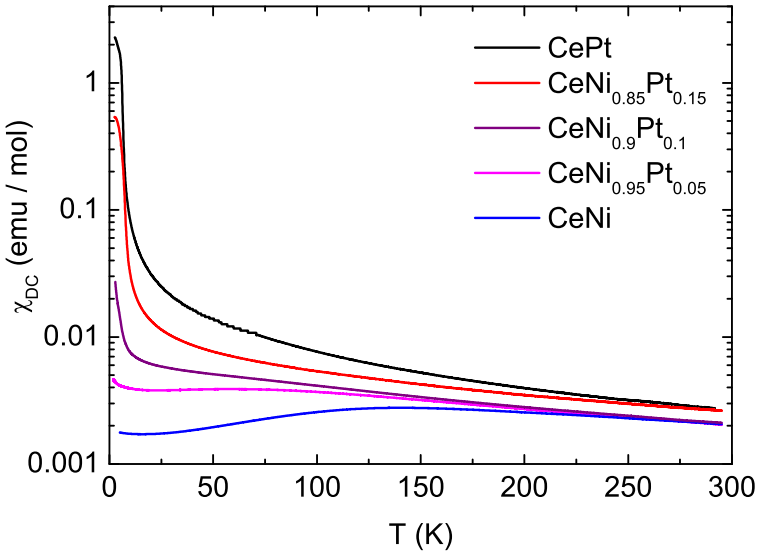

Figure 5.1: DC-susceptibility for $CeNi_xPt_{1-x}$ (x = 0, 0.85, 0.9, 0.95 and 1)

ties are shown in Fig. 5.1 for $CeNi_xPt_{1-x}$ with x = 0, 0.85, 0.9, 0.95 and 1. The same data in the low temperature range are shown in Fig. 5.2. At high temperatures the susceptibility follows the Curie-Weiss law:

$$\chi \simeq \frac{C}{T-\theta}.$$

The fit to this formula gives the values of paramagnetic moments μ_{eff},

$$\mu_{\text{eff}} = \sqrt{\frac{3k_BC}{N_A\mu_B^2}},$$

which are presented in Table 5.1 together with paramagnetic Curie-Weiss temperatures θ_p . The fits are illustrated in Fig. 5.3 for the compounds with x = 0, 0.85, 0.9.

The Curie temperature of magnetically ordered $CeNi_{0.9}Pt_{0.1}$ was determined using Arrott plots. For the samples CePt and $CeNi_{0.85}Pt_{0.15}$ the Curie temperatures were determined from temperature dependencies of DC susceptibility. They are in agreement with data from literature ([31]). We observe that the moments μ_{eff} are slightly reduced with increasing Ni content, but are still close (in our error range) to the free Ce^{3+} ion value of 2.54 μ_B. We mention, that paramagnetic moments μ_{eff} of course differ from the Kondo-screened low-temperature moments reported in Ref. [31].

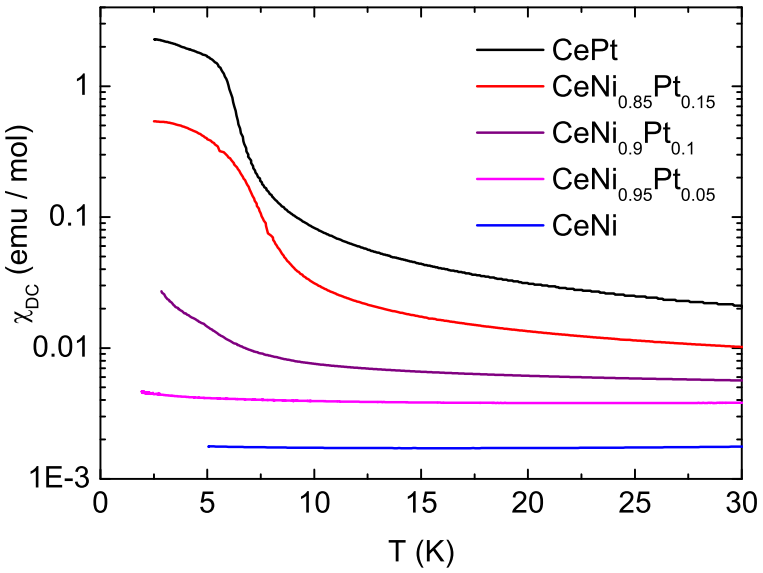

Figure 5.2: DC susceptibility for $CeNi_xPt_{1-x}$ (x = 0, 0.85, 0.9, 0.95 and 1) in the low temperature range.

The DC susceptibility of CeNi (Fig. 5.4) shows a broad maximum at 140 K corresponding to the Kondo temperature, in agreement with previous measurements [31]. For the $CeNi_{0.95}Pt_{0.05}$ sample, this maximum is shifted to 60 K (Fig. 5.4). An Arrott-plot-based calculation and AC-susceptibility measurements (in the temperature range 0.3–4 K) have revealed no magnetic order in these compounds. The small Curie-Weiss tail with an onset at $\sim$ 20 K yields effective moment μ_{eff}=0.12μ_B/f.u., resulting in an amount of 2.33% of a Ce^{3+} in this compound.

Our observations can be summarized as follows: (i) a substitution of Pt with Ni suppresses the magnetic order (Fig. 5.1), in agreement with literature data; namely, the DC susceptibility decreases monotonically by two orders in magnitude when the highest possible Ni concentration is reached; (ii) ferromagnetic transitions are well observed for CePt and for the sample with 85 % of Ni; however, only a weak shoulder around 4 K is seen for the sample with 90 % Ni content; (iii) the Curie temperature T_C is not a monotonic function of x: it approaches a maximum value of 6.5 K for x = 0.85, and drops down to zero at $x \geq 0.95$.

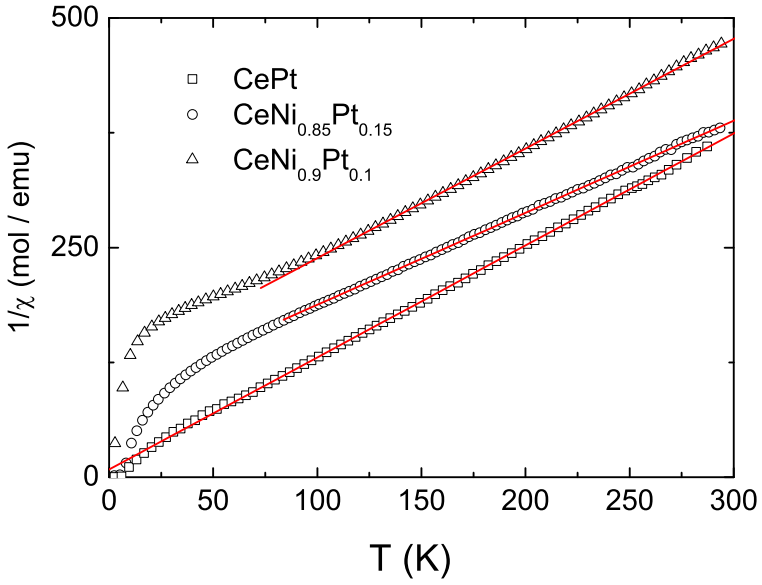

Figure 5.3: Inverse DC susceptibility for $CeNi_xPt_{1-x}$ ($x = 0, 0.85, 0.9$). Red curves show a high temperature fit with a Curie-Weiss law.

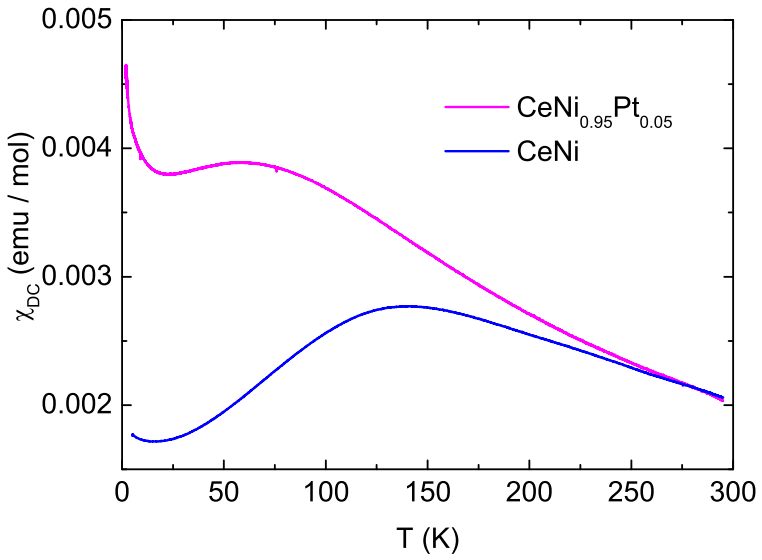

Figure 5.4: DC susceptibility of $CeNi_{0.95}Pt_{0.05}$ and of CeNi.

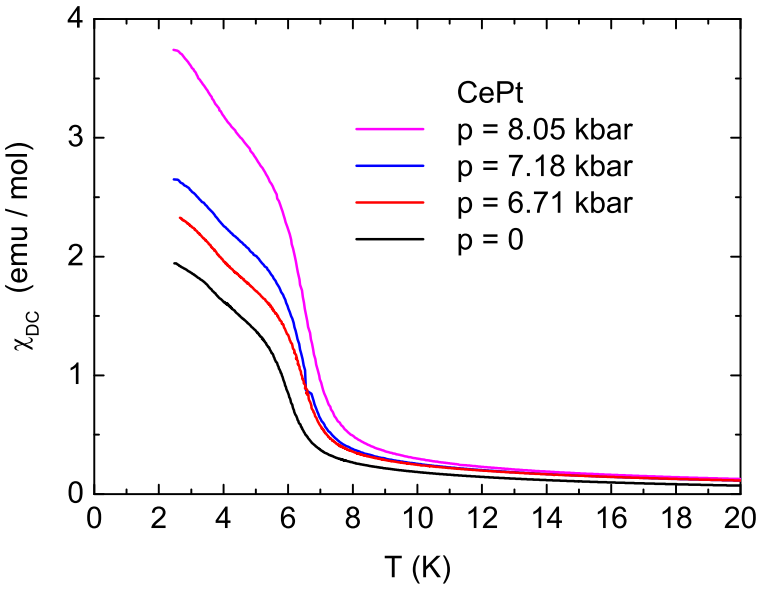

Figure 5.5: DC susceptibility for CePt at different applied pressure.

pressure, kbar	Curie temperature, K
0.0	6.00
6.7	6.35
7.2	6.40
8.1	6.53

Table 5.2: Pressure dependent Curie temperatures for CePt.

5.2 Measurements on CePt under hydrostatic pressure

Pressure measurements were performed with help of a clamp-cylinder pressure cell described in Chapter 2.

First, the pressure measurements were performed on CePt: it served as a test system, where results could be compared to the literature data. The temperature-dependent susceptibilities in the range of 2.5–20 K are shown in figure 5.5. Pressure dependent transition temperatures (obtained from Arrott plots) are given in Table 5.1. Our results are in agreement with those

reported by Larrea *et al.* [37]: T_C slightly increases with applied pressure (up to 0.8 GPa). In this range, the RKKY interaction dominates Kondo screening, and CePt orders ferromagnetically below T_C.

5.3 Pressure tuning of doped compounds $CeNi_{0.85}Pt_{0.15}$ and $CeNi_{0.9}Pt_{0.1}$ towards quantum critical point

It is known [37] that CePt can be driven to a quantum critical point (QCP) under high applied pressure. On the other hand, it is common to compare the changes under mechanical compression with the changes under *chemical pressure* exerted by alloying with isovalent atoms of different size [31, 30, 40]. The overview of literature data given in Chapter 4 shows that when Pt is substituted with Ni, $T_C(x)$ indeed behaves similar to $T_C(p)$ measured in pressure experiments. However, doping only is not able to drive the system directly to the QCP. Above $x_c \approx 0.9$, where T_C is still finite (cf. Fig. 4.4), the magnetic signal abruptly disappears [31, 30]: this indicates the importance of electronic effects in the alloys. As a consequence, there is no direct one-to-one correspondence to the pressure experiments. However, the expectation is that T_C can still be driven to zero (i.e. to the QCP) if only the pressure is high enough.

We have produced two samples, $CeNi_{0.85}Pt_{0.15}$ and $CeNi_{0.9}Pt_{0.1}$. In Figures 5.6 and 5.7, we plot the measured susceptibility data (χ_{DC} versus T) for these samples. As expected, with applied pressure the susceptibilities are gradually reduced, indicating weakened magnetic order.

The Curie temperatures T_C, obtained using Arrott plots, are shown in Fig. 5.8. Details of the method are discussed in the following chapter section. In comparison to CePt, the two doped compounds are closer to the QCP. Thus, a relatively small pressure (about 1 GPa) is enough to push T_C towards zero. The critical pressure p_c is smaller for the compound with a larger amount of Ni. The dashed lines show the $T_c(p)$ as predicted by the spin-fluctuation theory of Hertz [18] and Millis [19]. For the case of three-dimensional FM ($d = 3, z = 3$), one gets $T_c \propto |p_0 - p|^{3/4}$.

Larrea *et al.* [37] discussed an alternative to the spin-fluctuation theory scenario on how the system approaches the quantum critical point. They suggested to relate a ferromagnetic instability close to the

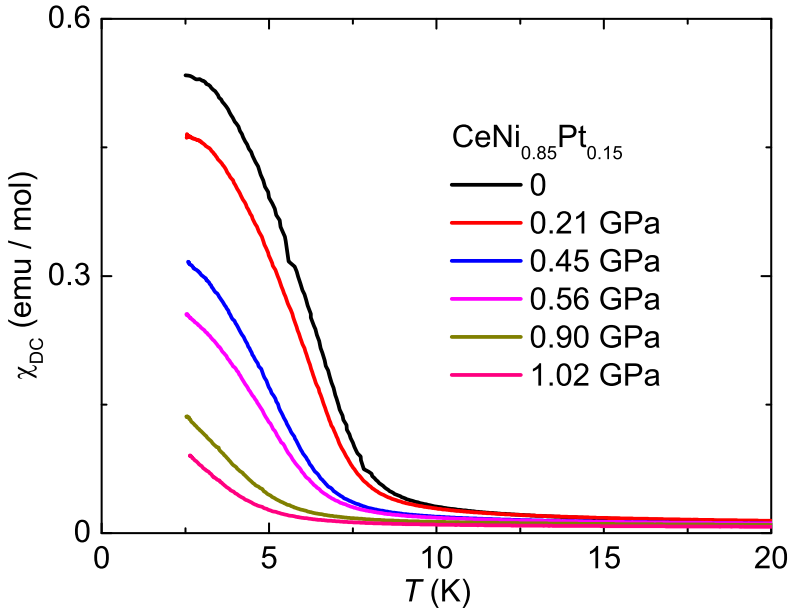

Figure 5.6: DC susceptibility versus T for $CeNi_{0.85}Pt_{0.15}$ at different applied pressure.

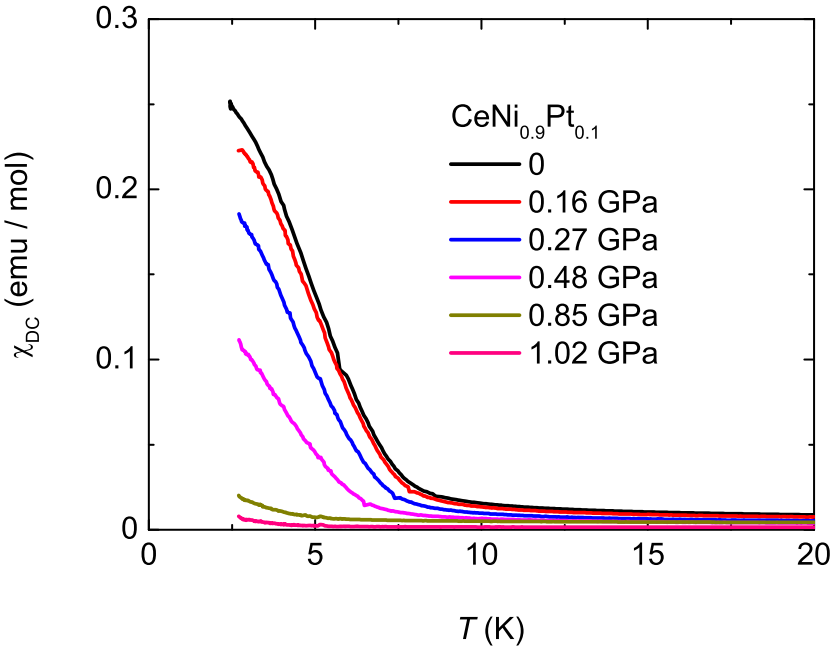

Figure 5.7: DC susceptibility versus T for $CeNi_{0.9}Pt_{0.1}$ at different applied pressure.

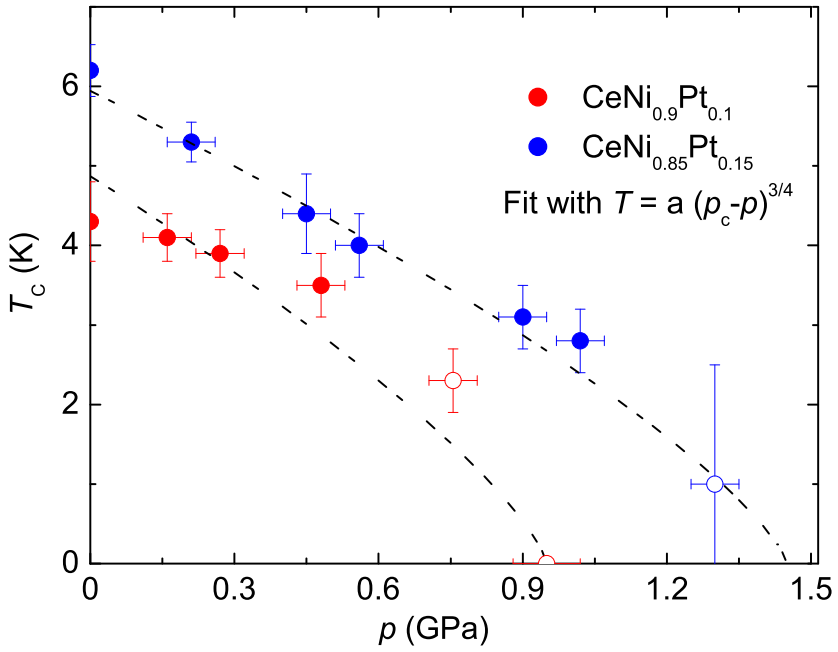

Figure 5.8: T_C versus p for $CeNi_{0.85}Pt_{0.15}$ and $CeNi_{0.9}Pt_{0.1}$.

QCP with soft spin-wave modes in an anisotropic quasi-two-dimensional material. For the CePt compound, authors of Ref. [37] have shown that an important contribution to the resistivity arises from scattering of electrons by spin-waves with a gap in the dispersion relation: $\omega(\mathbf{k}) = \Delta + D\mathbf{k}^2$ (here D is the spin-wave stiffness). The origin of the gap Δ comes from the strong anisotropy of the CrB crystal structure (cf. Fig. 5 of Ref. [37]), consisting of layers of Ce triangular prisms, containing Pt atoms stacked along the c axis: such a structure suggests the reduced effective two-dimensional character of magnetic fluctuations. Under this assumption, fits of T_C curves when approaching the QCP (see Figs. 5.9, 5.10) may be obtained within the two-dimensional anisotropic ferromagnetic Heisenberg model with a gap in the spectrum of the spin-wave excitations. A vanishing of T_C at a critical point p_c in this model can be obtained under the assumption that the pressure dependent gap, $\Delta(p) = \Delta_0|p - p_c|$, approaches zero at the same critical pressure. Within the random phase approximation [43], the appropriate relation for T_C reads as

$$k_B T_c = \frac{2\Gamma}{\pi} \ln^{-1}\left(1 + \frac{\Gamma}{\Delta_0|p - p_c|}\right),$$

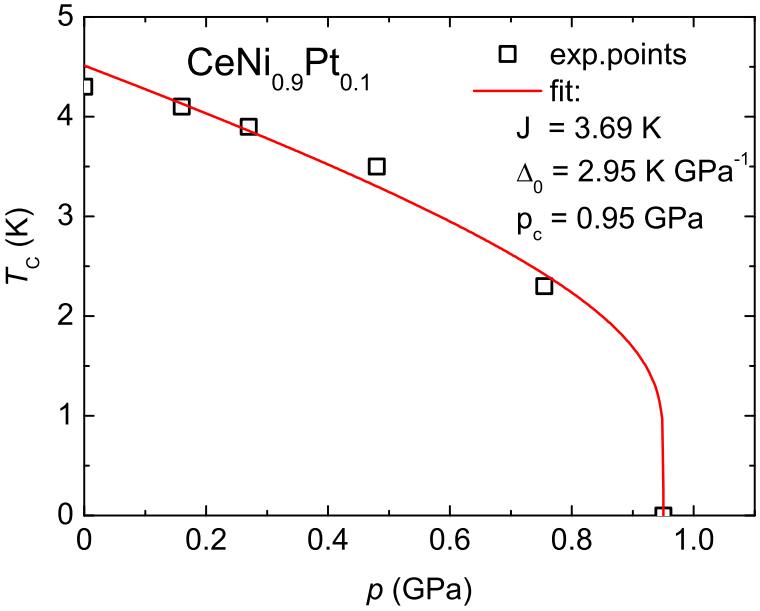

Figure 5.9: T_C versus p $CeNi_{0.9}Pt_{0.1}$ together with a fit within 2D FM anisotropic Heisenberg model.

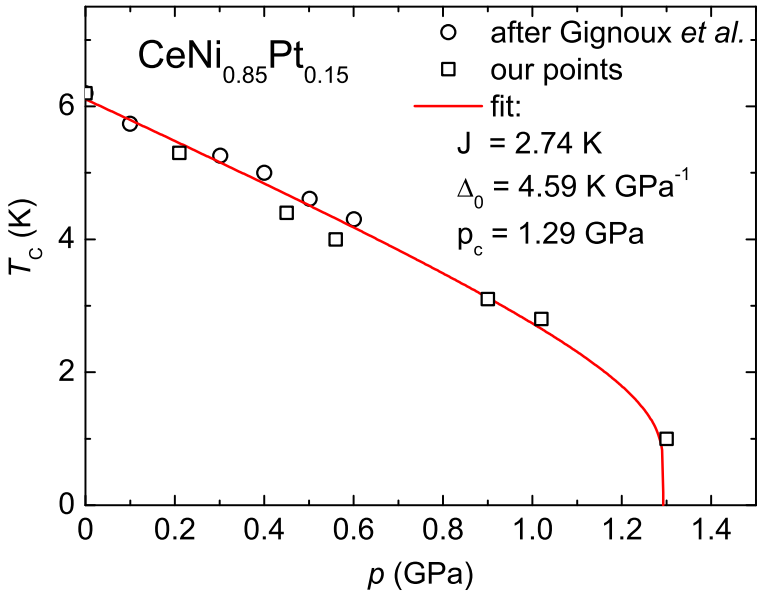

Figure 5.10: T_C versus p for $CeNi_{0.9}Pt_{0.1}$ together with a fit within 2D FM anisotropic Heisenberg model.

such that $T_c \to 0$ when $\Delta = \Delta_0|p - p_c| \to 0$ at $p \to p_c$, and the parameter Γ related to the spin-wave stiffness ($\Gamma \propto D$) is assumed to be constant close to the QCP. According to Larrea *et al.* [37], one may tentatively relate the vanishing gap with f electron wave functions being less anisotropic under high applied pressure, because of their increased hybridization with conduction d electrons of Pt (and Ni) which have quenched orbital magnetic moments.

Fits of experimental points to the above formula (with adjustable parameters Γ, Δ_0, and p_c) are shown in Figures 5.9 and 5.10. The found critical pressures p_c are 0.95 GPa for the $CeNi_{0.9}Pt_{0.1}$ compound, and 1.29 GPa for the $CeNi_{0.85}Pt_{0.15}$ compound. Δ_0 is almost the same value for all samples. The ferromagnetic exchange constants ($J = \Gamma/\pi$) were estimated as $J(x = 0.9) = 3.69$ K and $J(x = 0.85) = 2.74$ K, respectively.

5.4 Arrott-plot method

A widely used experimental tool for evaluating a ferromagnetic ordering temperature is the Arrott-plot method [41]. It is based on the Weiss molecular field theory. In case of a ferromagnet, the dependences M^2 versus H/M at constant temperatures (isotherms) should be a set of parallel straight lines and the isotherm crossing the origin corresponds to the Curie temperature. However, for disordered ferromagnets the region of validity of Weiss expansion comprises small values of magnetisations and the $M^2(H/M)$ plots are curved. Besides, the $M^2(H/M)$ dependence can not be measured down to $M^2 = 0$. Yeung *et al.* [42] proposed to interpolate the curves intercept with the H/M axis or the M^2 axis using the slope of the measured isotherm at small H field for $T > T_C$. Consider the isotherms with $T < T_C$. The intercept is negative at this temperatures. According to Arrott [41] for $T < T_C$ high field curve part have been extrapolated. Within this approach one can calculate lower and upper estimates for the Curie temperature T_C: the isotherms with temperatures T higher than T_C should intersect the horizontal axis (H/M), and isotherms with lower T compared to T_C intersect the vertical axis (M^2) of the M^2–H/M diagram.

The Arrott plot for the sample $CeNi_{0.85}Pt_{0.15}$ under pressure of 0.56 GPa is shown in Fig. 5.11. From the plotted isotherms it is seen that T_C lies below 5 K, and above 3 K. A more precise determination is presented in Fig. 5.12. From Fig. 5.11 one can extract the abscissa intercepts h_k. The straight line $h(T) = a + bT$ (see Fig. 5.14) gives the value of T_C from the condition $h(T) = 0$. The Curie temperature is found from the condition $h(T_c) = 0$. Thus, we get $T_C = 4.0$ K.

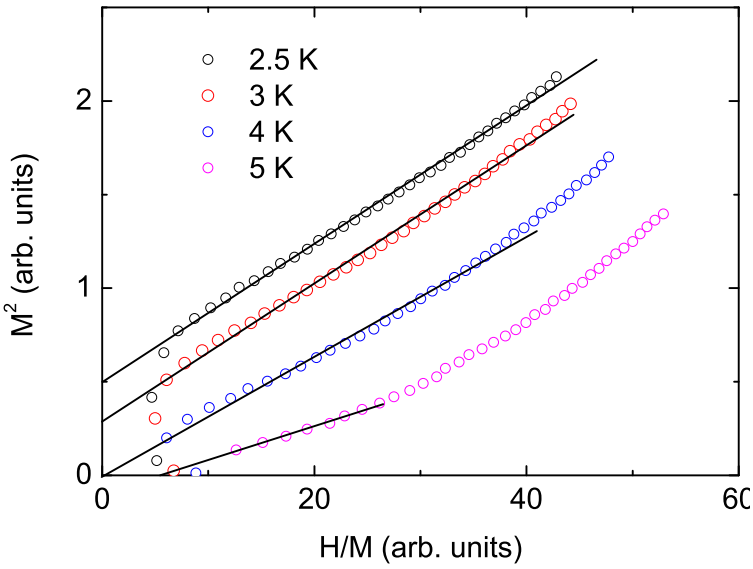

Figure 5.11: Arrott plots for $CeNi_{0.85}Pt_{0.15}$ at $p = 0.56$ GPa at different temperatures.

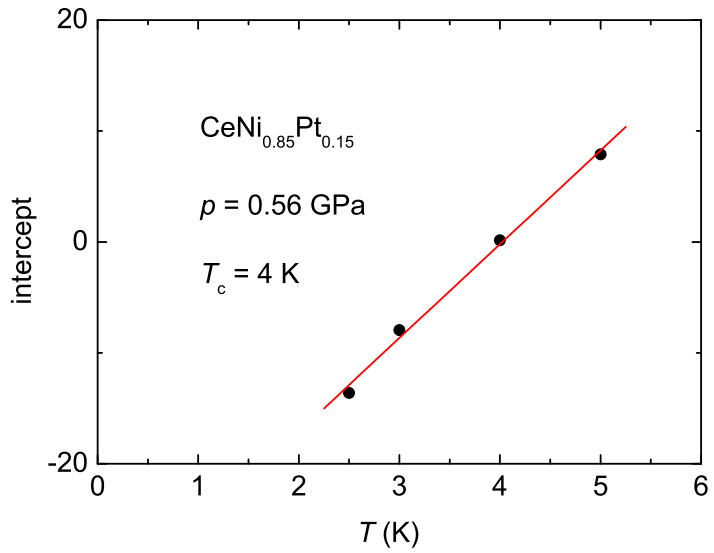

Figure 5.12: Intercepts of Arrott plots versus T for $CeNi_{0.85}Pt_{0.15}$ at $p = 0.56$ GPa. $T_C = 4$ K.

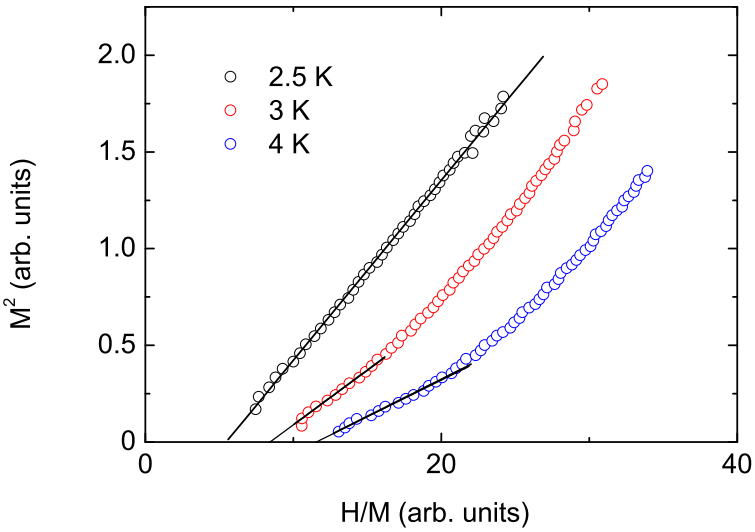

Figure 5.13: Arrott plots for $CeNi_{0.85}Pt_{0.15}$ at $p = 1.3$ GPa at different temperatures

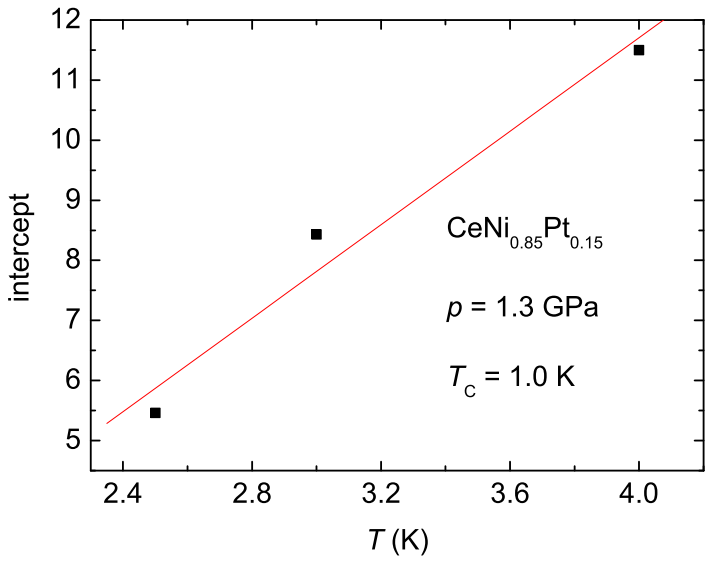

Figure 5.14: Intercepts of Arrott plots versus T for $CeNi_{0.85}Pt_{0.15}$ at $p = 1.3$ GPa. $T_C = 1.4 \pm 0.4$ K.

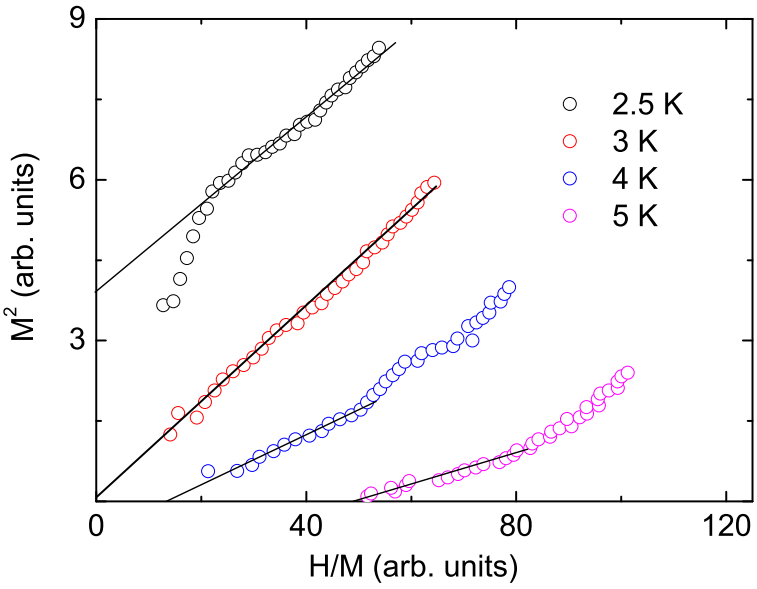

Figure 5.15: Arrott plots for $CeNi_{0.9}Pt_{0.1}$ at $p = 0.48$ GPa at different temperatures.

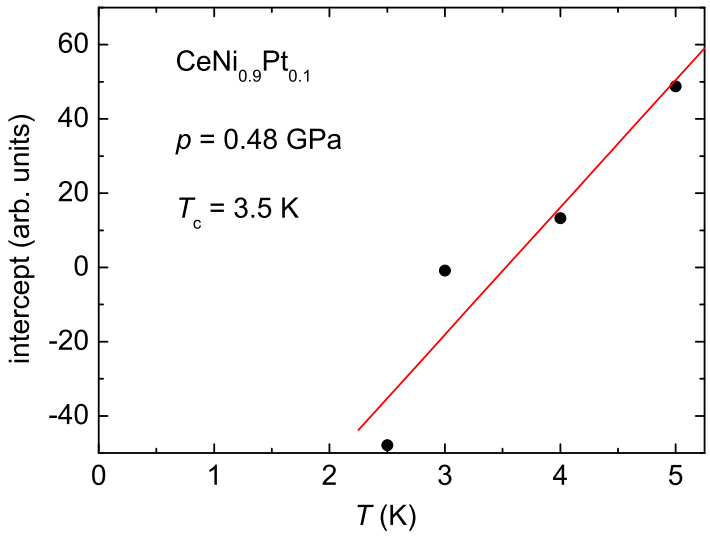

Figure 5.16: Intercepts of Arrott plots versus T for $CeNi_{0.9}Pt_{0.1}$ at $p = 0.48$ Pa. $T_C = 3.5 \pm 0.4$ K.

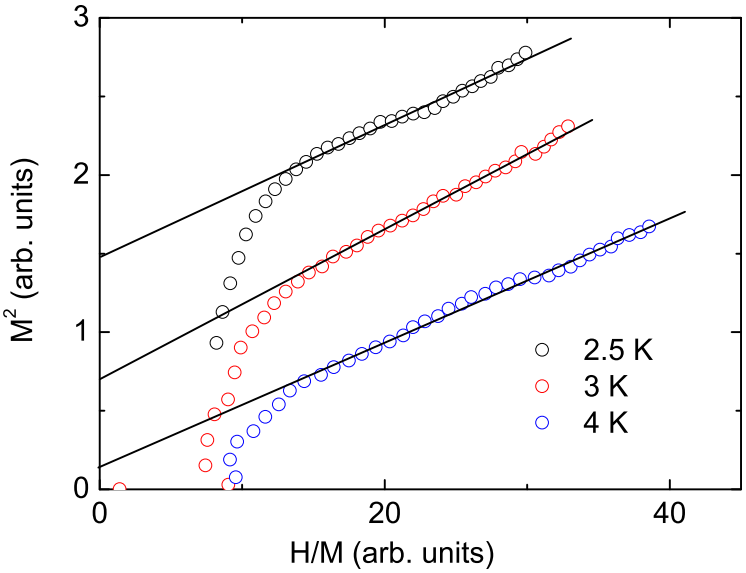

Figure 5.17: Arrott plots for $CeNi_{0.9}Pt_{0.1}$ at $p = 0.16$ GPa at different temperatures.

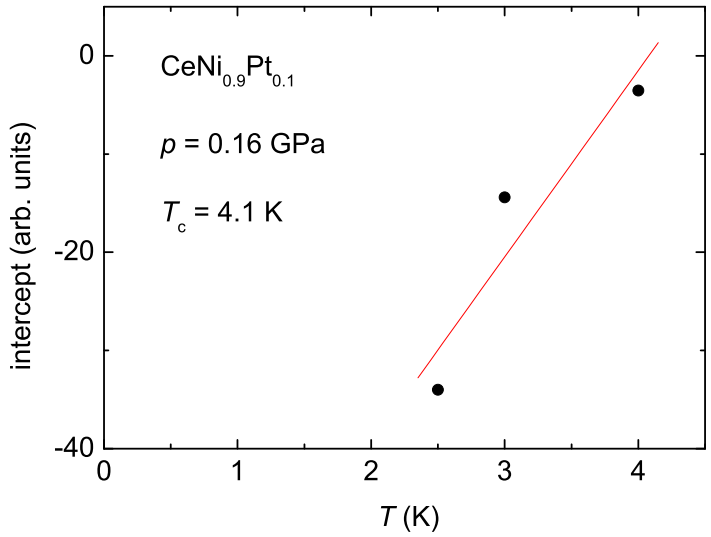

Figure 5.18: Intercepts of Arrott plots versus T for $CeNi_{0.9}Pt_{0.1}$ at $p = 0.16$ GPa. $T_C = 4.1 \pm 0.3$ K.

When T_C is below the temperature that we can read with VSM, the Arrott plot does not yield a finite M^2 value for $H/M \to 0$. In this case, the method can not be applied straightforwardly. In Fig. 5.13, we present an example of an Arrott plots for the sample $CeNi_{0.85}Pt_{0.15}$ at large pressure p = 1.3 GPa. All isotherms correspond to temperatures, which lie above the Curie temperature at this pressure value.

Nevertheless, we were able to extrapolate rather relatively T_C from the linear fit function $h(T)$. Although, we approach T_C from above.

For the sample $CeNi_{0.9}Pt_{0.1}$ the Arrott plots show a more pronounced curvature, their intercepts were determined from the lower part of the curves. One example of these calculations is presented in Figs. 5.15 and 5.16. From Fig. 5.15 it is seen that Curie temperature a bit higher than 3 K, the fit gives T_C = 3.5 K. One more example of Arrott plots for $CeNi_{0.9}Pt_{0.1}$ at 0.16 GPa is shown in Figs. 5.17, 5.18. T_C was found to be 4.1 K.

5.5 Pressure and doping diagram for $CeNi_xPt_{1-x}$

The volume change by external pressure and by chemical doping can be compared if bulk modulus is known. The isothermal bulk modulus is given by following relation:

$$B_T = -V \left.\frac{\partial P}{\partial V}\right|_T, \text{where } P = -\left.\frac{\partial F}{\partial V}\right|_T, \text{and } B_T = V \left.\frac{\partial^2 F}{\partial V^2}\right|_T$$

Here P is the pressure and V is the volume. F is the free energy. Bulk moduli depend on pressure, temperature and volume.

For polycrystalline and/or composite metallic compounds the modulus can be described empirically by the following relation:

$$B_{VR} = \frac{B_{\text{Voigt}} + B_{\text{Reuss}}}{2}$$

where

$$B_{\text{Voigt}} = \sum_i f_i B_i \ ; \ B^{-1}_{\text{Reuss}} = \sum_i \frac{f_i}{B_i} \ ; \ \sum_i f_i = 1,$$

f_i are volume fractions of different phases, B_i are the respective bulk moduli [44].

Here we adopt this method with certain modifications and apply it to Ce-based alloys $CeNi_xPt_{1-x}$ [45]. Namely, since ions in intermetallic compound are tightly linked by chemical bonds, the volume fractions f_i were substituted by fractions x_i. Indeed, we have found this approximation to work quite well,

as can be seen from Table A1 (see Appendix), where experimentally determined values of B, calculated B_{Voigt}, B_{Reuss} and B_{VR} for different compounds are given. In Table 5.3, calculated values of bulk moduli for $CeNi_{0.9}Pt_{0.1}$ and $CeNi_{0.85}Pt_{0.15}$ alloys are presented. The B values of pure metals (Ce, Ni, Pt) have been taken from Ref. [46].

The temperature dependence of the bulk modulus and magnetic effects are neglected. The pressure dependence is taken into account in the form of Murnaghan equation:

$$B = B_0(p=0) + p\frac{dB}{dp}\bigg|_{p=0}$$

and, for cell volume one has:

$$\frac{V}{V_0} = \left[1 + \frac{\frac{dB}{dp}|_{p=0}}{B_0}p\right]^{-1/\frac{dB}{dp}|_{p=0}}.$$

For the $\frac{dB}{dp}$ the value of 5 was used, which was found empirically for most compounds [45].

compound	B_{VR} (GPa)	B_{Voigt} (GPa)	B_{Reuss} (GPa)
$CeNi_{0.9}Pt_{0.1}$	74.0	39.1	108.9
$CeNi_{0.85}Pt_{0.15}$	74.7	39.1	110.3

Table 5.3: Bulk modulus for $CeNi_{0.9}Pt_{0.1}$ and $CeNi_{0.85}Pt_{0.15}$ compounds.

We summarize our results on Curie temperature dependence of the cell volumes of $CeNi_xPt_{1-x}$ in Fig. 5.19. In addition, we present data for CePt after Larrea *et al.* [37], Gignoux [40] *et al.*, Itoh [38] *et al.*, as well as data on $CeNi_xPt_{1-x}$ compounds after Gignoux *et al.* [31, 40]. Both Ni doping and application of hydrostatic pressure reduce the unit-cell volume.The transition temperature first increases slightly with decreasing the cell volume (and increasing pressure, respectively), and then drops to zero when approaching the QCP. Our experimental points for the pure CePt compound are in very good agreement with data of Larrea and Gignoux, whereas that from Itoh lie on the curve for the doped samples.

Our data for $CeNi_{0.85}Pt_{0.15}$ are in a good agreement with data of Gignoux *et al.* [40]. However, we have managed to achieve higher pressure values and obtained a complete set of data points, so that the QCP can be reached. Our conclusions can be summarized as follows: (i) close to the QCP a small

compression is enough to diminish T_C substantially; (ii) close to the QCP pressure suppresses the magnetic order faster than substituting Pt with Ni; (iii) doping with Ni compresses the unit cell and affects the electronic structure of the alloys.

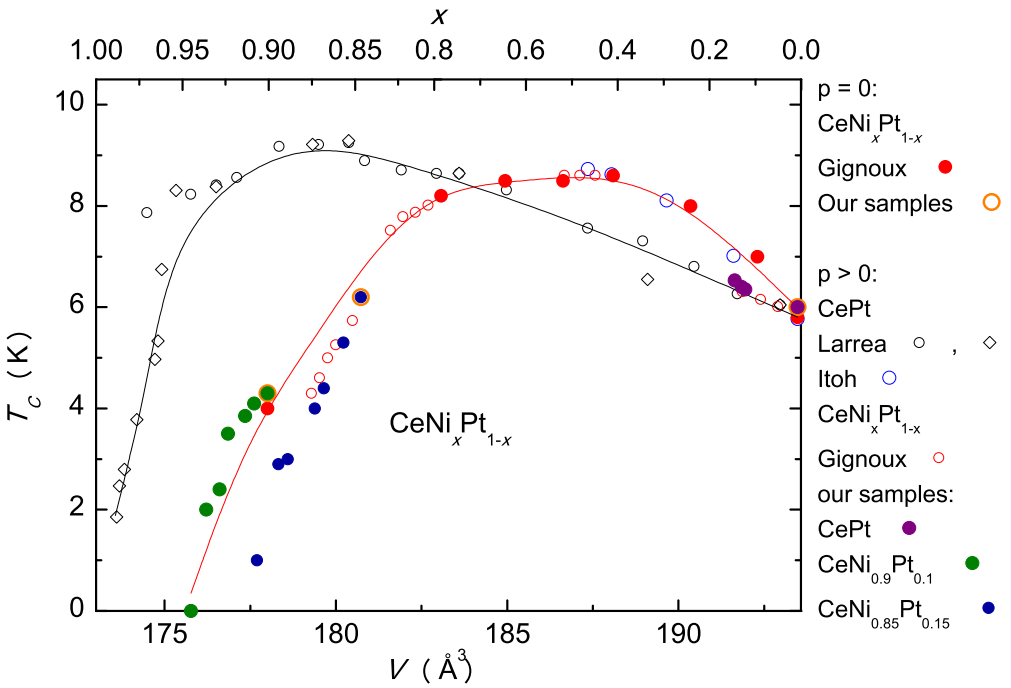

Figure 5.19: Pressure and doping diagram for $CeNi_xPt_{1-x}$ compounds. The data for CePt under pressure ○ - after Larrea [37], and ○ - after Itoh [38]. The data for doped $CeNi_xPt_{1-x}$ ● are from Gignoux [31], and the data for $CeNi_xPt_{1-x}$ under external pressure - ○ after Gignoux [40].

Chapter 6

CePdAl: a heavy fermion compound on a Kagomé-like lattice

6.1 Experimental data

Recent measurements [47, 48, 49] revealed unusual properties of CePdAl, which is the first known heavy-fermion Ce-based system on a Kagomé-like lattice. Its crystal structure is of ZrNiAl-type (hexagonal space group P62m, see Fig. 6.1 [49], where the magnetic Ce ions form a network of equilateral triangles in the *ab* plane, similar to the Kagomé lattice. The number of nearest neighbors of each Ce atom is 4 in this compound, as in the Kagomé lattice. However, the hexagons formed by Ce are distorted so that the number of *next nearest Ce neighbors* is 2, although this number is 4 in the Kagomé lattice. The nearest neighbor (NN) distances between Ce atoms are 4.233 Å along the *c*-axis, and 3.722 Å in the *ab*-plane. The shorter NN distance in the *ab*-plane suggests strong two-dimensional magnetic correlations.

The electronic specific-heat coefficient of CePdAl is $\gamma = 270$ mJ/K^{2}mol. The resistivity shows a behavior typical for dense Kondo systems: a $\ln T$ dependence with a minimum around 20 K. A broad maximum at 4 K, and the steep decrease is observed below Néel temperature $T_N = 2.7$ K [50].

The most remarkable property of CePdAl is a partially ordered magnetic state. The magnetic structure is schematically shown in Fig. 6.2. Neutron diffraction measurements on powder samples have shown that two thirds of the Ce moments are ordered antiferromagnetically below $T_N = 2.7$ K with a propagating vector $\mathbf{k} = (1/2, 0, 0.351)$, while one third of the Ce moments remains paramagnetic, as shown in Fig. 6.2. Furthermore, the magnetic

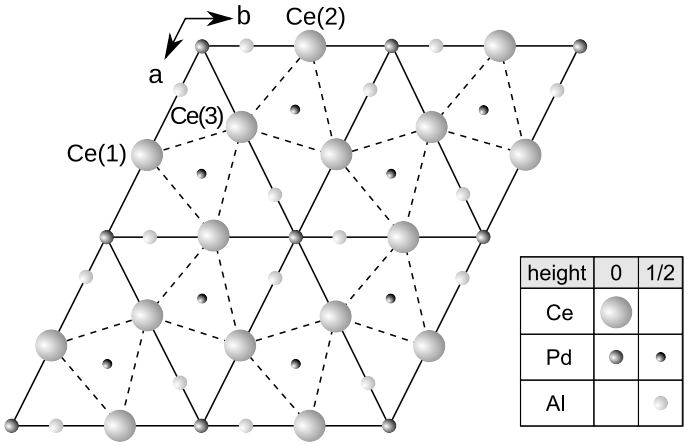

Figure 6.1: The crystal structure of CePdAl (ZrNiAl type) plotted as a view onto the hexagonal *ab* plane [49]. The heights of the atoms are in units of $z = c$. Dashed lines illustrate the triangular lattice of the magnetic Ce atoms.

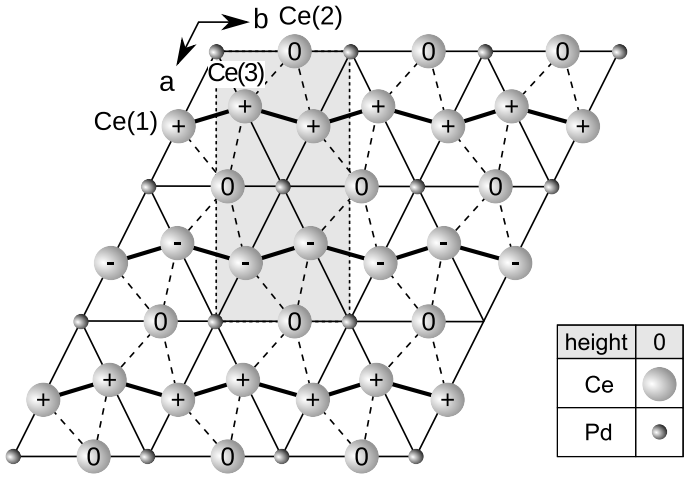

Figure 6.2: The basal plane of the magnetic structure of CePdAl for 1.3 K $< T <$ 2.7 K [49]. The magnetic Ce moments are partly ordered, parallel (+) and antiparallel (–) to the *c*-axis, and partly disordered (0). The unit cell for the orthorhombic description of the crystal structure is highlighted by the gray color.

structure is incommensurate along the c-axis. The magnetic susceptibility of CePdAl follows a Curie-Weiss law above 120 K. The effective magnetic moment of 2.53 μ_B is close to the Ce^{3+} free-ion value of 2.54 μ_B and the paramagnetic Curie temperature is $\Theta_p = -34$ K [49].

6.2 Frustrated Kondo model

In order to explain the partially ordered state in CePdAl, the two-dimensional Ising model accounting for the Kondo effect and two kinds of exchange interactions on a Kagomé-like lattice has been proposed by Núñes-Regueiro *et al.* [50]. The model Hamiltonian (frustrated Kondo model) includes the nearest neighbor and the next-nearest neighbor interactions between Ce atoms (J_1 and J_2, respectively) as follows:

$$H = \sum_i \Delta_i(T) \mid \mu_i^z|^2 + \frac{1}{2} \sum_{1st\ nn.} J_1 \vec{\mu_i^z} \vec{\mu_j^z} + \frac{1}{2} \sum_{2nd\ nn.} J_2 \vec{\mu_i^z} \vec{\mu_j^z}$$

where $\Delta_i(T)$ is the energy difference between the completely screened Kondo state $\mu_i = 0$ and the magnetic Ce state $\mu_i \neq 0$. A schematic view of the magnetic phase diagram of this model is given in Fig. 6.3. The paths of exchange interactions J_1 and J_2 are presented as solid and dotted lines, respectively. The magnetic structure shows up in the regions of the phase diagram where conditions $J_1 > 0$ and $J_2 < 0$ are satisfied. This structure is strongly affected by frustration of the antiferromagnetic interaction J_2. Oyamada *et al.* [51] have found that the Kondo effect and/or a distortion of the Kagomé lattice play an important role in extending the region where the partially ordered state is stable at $T = 0$ (light shaded area). The lower right-hand side of the phase diagram is the region where CePdAl exists. The conclusions of Ref. [51] suggest that a cancellation of magnetic moments by the Kondo effect relieves the frustration of the Kagomé-like lattice and that the partially ordered state is stable down to $T = 0$.

6.3 Effect of hydrostatic pressure on magnetic order in CePdAl

The discussion of CePt and $CeNi_xPt_{1-x}$ presented in previous chapters has given an additional example that heavy-fermion systems could be driven to the quantum critical point (QCP) by applying hydrostatic pressure, as a result of Kondo screening dominating the RKKY interaction at the critical

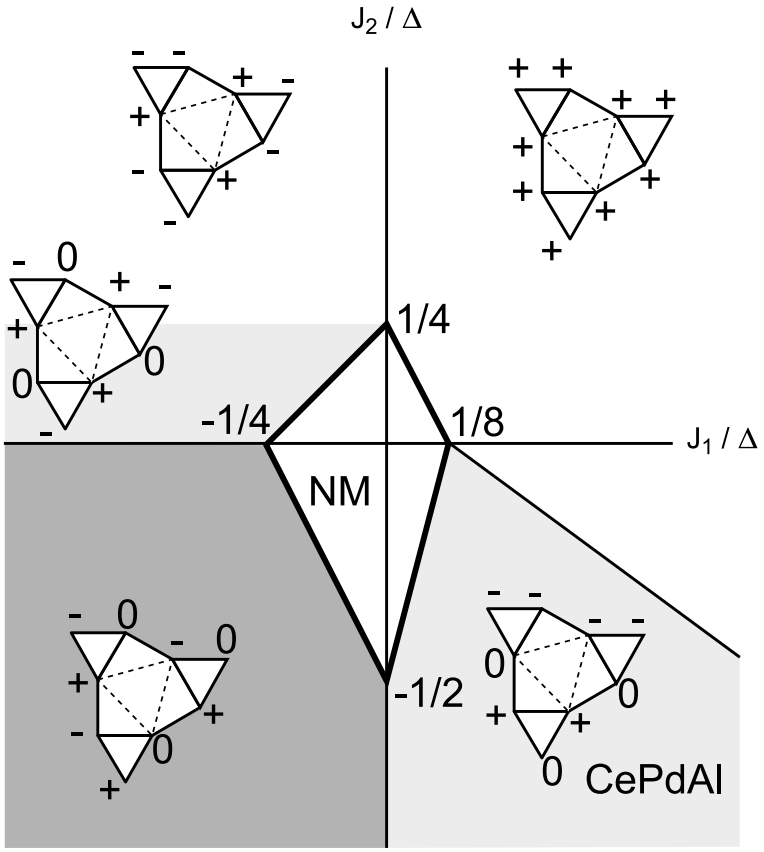

Figure 6.3: Schematic view of the magnetic phase diagram reported by Dolores Núñes-Regueiro *et al.* using the model Hamiltonian approach [50, 51]. The magnetic structures at 0 K are shown. NM indicates absence of the magnetic order. The dark shaded area $J_1 < 0$, $J_2 < 0$ is the region where the partially ordered state is stable at 0 K in the classical Ising spin system on the Kagomé lattice without the Kondo effect [51]. The light shaded areas are the extended regions where the partially ordered state is stable at 0 K due to the Kondo effect and/or distortion of the Kagomé lattice.

region. The same is valid for the CePdAl compound. For example, specific-heat measurements on CePdAl under pressure [49, 52] have shown that T_N is monotonically reduced down to 1.7 K at 0.9 GPa [49]. Non-Fermi-liquid behaviour has been reported by Akamaru *et al.* [53], who observed a $T^{1.5}$ dependence of the resistivity above 0.6 GPa. The hydrostatic pressure effect on CePdAl has been thoroughly studied by Goto *et al.* [54], their work is discussed further in more detail.

Goto *et al.* [54] measured susceptibility $\chi(T)$ under high pressures up to 1.2 GPa to examine the pressure induced magnetic instability. At ambient pressure, in the temperature window below 8 K, $\chi(T)$ increases with decreasing T, shows a broad maximum associated with T_N and then drops. With increasing pressure, the maximum shifts downwards to the low temperature side. Above 1.0 GPa, the maximum disappears and an anomaly corresponding to T_N could not be found down to 0.6 K. We will show in Chapter 7 that the QCP, where the antiferromagnetic order disappears, is found in our work at $p_c = 0.95$ GPa. Above the critical pressure, $p > p_c$, the susceptibility χ grows with decreasing temperature. As has been noted by Goto *et al.* [54], this is a manifestation of the non-Fermi-liquid behavior originating from quantum fluctuations.

Goto *et al.* [54] performed specific-heat measurements $C(T)$ at low temperatures down to 0.4 K and under high pressures up to 1.3 GPa. The magnetic contribution, C_{mag}, to the specific heat was obtained from the difference between the data of CePdAl and non-magnetic CeNiAl compound. The authors observed a λ-type anomaly at 2.7 K and found the magnetic entropy to be $S_{mag} = 0.38R\ln 2$ at T_N. By applying pressure, the peak position corresponding to T_N shifts to lower temperatures and vanishes for $p \geq 0.83$ GPa. At 1.3 GPa, C_{mag}/T increases gradually with decreasing T, reaching 0.48 J/mol K^2 at 0.4 K. C_{mag}/T for $p \geq 0.95$ GPa exhibits a $-\ln T$ dependence in the temperature range $T < 3$ K, indicating non-Fermi-liquid behavior.

These studies on CePdAl motivated us to investigate the effect of doping (chemical pressure) on the magnetic order in $CePd_{1-x}Ni_xAl$, where the control parameter driving a system to the QCP point is the Ni concentration x. Our experimental results on quantum critical behaviour of doped $CePd_{1-x}Ni_xAl$ compounds will be discussed in the following Chapter 7.

Chapter 7

Quantum phase transition in $CePd_{1-x}Ni_xAl$ compounds

This chapter is devoted to the heavy-fermion alloys $CePd_{1-x}Ni_xAl$: here we confirm that chemical pressure can guide the system to the quantum phase transition. This is in contrast to $CeNi_xPt_{1-x}$ alloys, where such a possibility was impeded by competing electronic structure effects.

7.1 Specific-heat of CePdAl

In this section we discuss heat-capacity measurements on CePdAl in a broad temperature range up to 300 K. For the rare-earth intermetallic Ce, the specific-heat usually shows a broad Schottky anomaly due to the splitting of the Hund's rule J=5/2 multiplet by the crystalline electric field (CEF) [55, 56]. An analysis of Schottky anomaly gives information about a multiplet structure of the electronic levels of the rare earth ions which is required for the description of electronic and magnetic properties.

Specific-heat measurements for CePdAl have been performed at the IFP, Forschungszentrum Karlsruhe with help of the PPMS[1] setup in the temperature range 0.3–300 K. The heat capacity of CePdAl and of the isomorphic non-magnetic compound LuPdAl are presented in Fig. 7.1. The latter serves as a reference compound for the lattice contribution to the specific-heat.

[1]Physical Property Measurement System from `Quantum Design (www.qdusa.com)`.

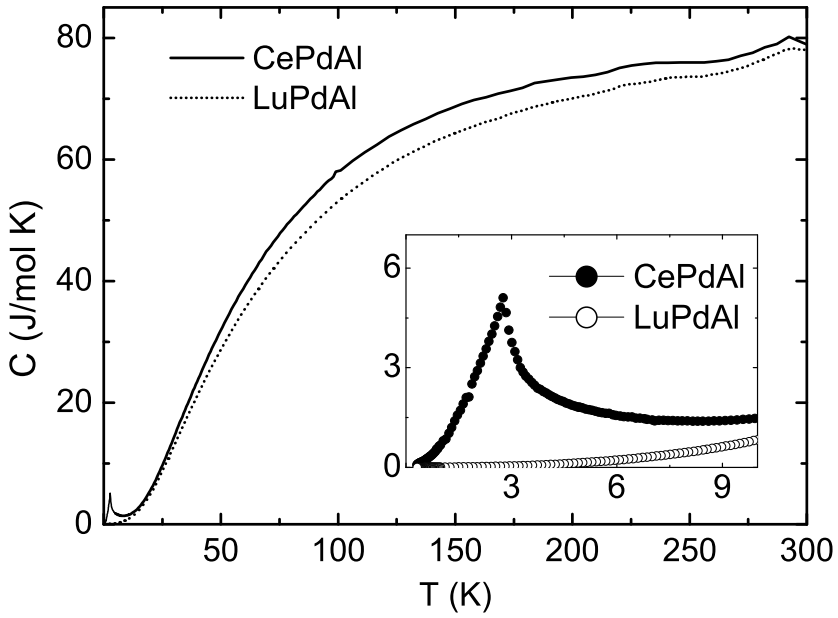

Figure 7.1: Specific-heat of CePdAl and LuPdAl. The inset shows the low-temperature region in detail.

A λ-anomaly at Néel temperature $T_N = 2.7$ K is observed for CePdAl, which is in agreement with Goto *at al* [54]. Apart from that, a relevant increase of the CePdAl specific-heat is seen with regard to that of LuPdAl, especially in the temperature interval 100–200 K. From

$$C_{\mathrm{mag}} = C_{\mathrm{CePdAl}} - C_{\mathrm{LuPdAl}},$$

we have calculated the magnetic contribution to the entropy

$$S_{\mathrm{mag}} = \int_0^T (C_{\mathrm{mag}}/T)\, dT,$$

which is plotted in the upper Fig. 7.2 for CePdAl.

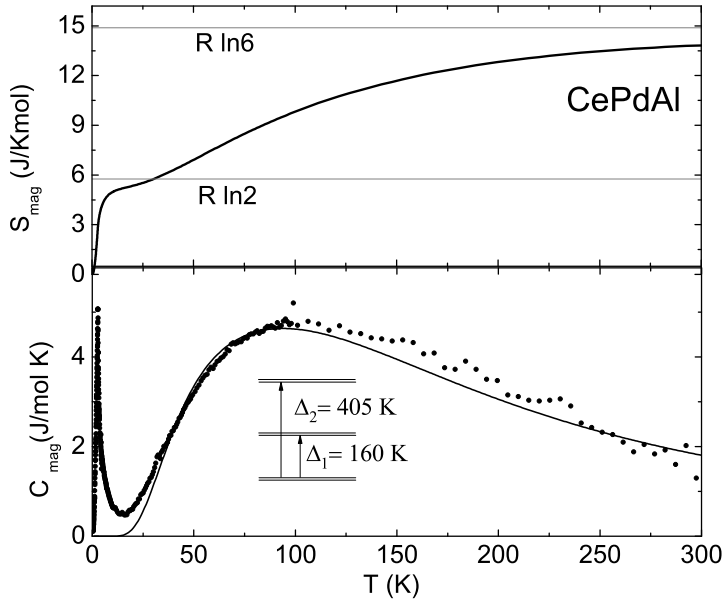

Figure 7.2: Magnetic entropy and magnetic specific-heat versus T of CePdAl. The solid line corresponds to a theoretical fit in the paramagnetic phase within the crystalline electric field (CEF) scheme with $\Delta_1 = 160$ K and $\Delta_2 = 405$ K.

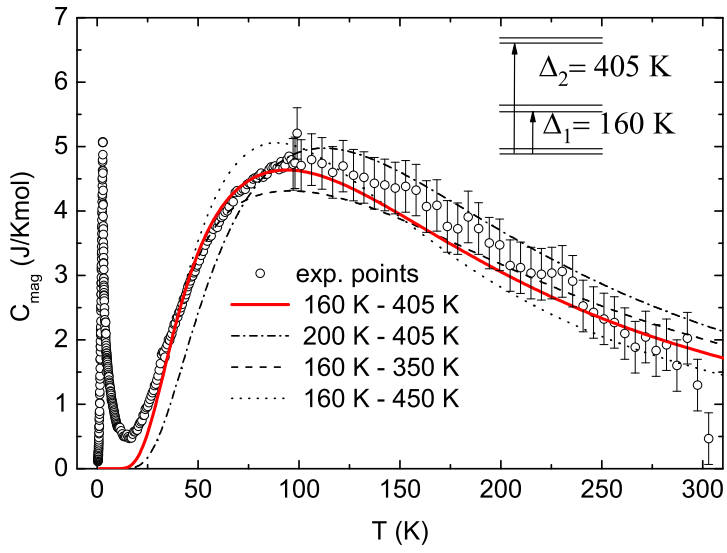

Figure 7.3: Simulated curves for different Δ_1 and Δ_2 values. The best fit to the experimental points was obtained with $\Delta_1 = 160$ K and $\Delta_2 = 405$ K.

The magnetic contribution to the specific-heat C_{mag} exhibits a broad Schottky-type anomaly around ~ 100 K. Due to the low-symmetry site occupied by the Ce^{3+} ion, the $J = 5/2$ ground multiplet splits into three crystal-field doublets. Within the CEF scheme [57], the best fit has been obtained assuming that the excited states are separated from the ground state by energy gaps $\Delta_1 = 160$ K and $\Delta_2 = 405$ K. To compare, we plot simulated curves with different Δ_1 and Δ_2 in Fig. 7.3. Error bars above the magnetic transition originate from commensurable values of C for CePdAl and LuPdAl in high temperature range, where the precision of measurements was about 0.5 %. We mention, that the most direct method to determine CEF levels would be inelastic neutron scattering measurements. Unfortunately, no information of such measurements is available. The entropy at the Néel temperature is smaller than $R \ln 2$, indicating the influence of Kondo screening [55]. At 300 K, S_{mag} is slightly lower than $R \ln 6$ corresponding to the total degeneracy of the $J = 5/2$ multiplet due to thermal population of the excited doublets.

7.2 Tuning of magnetic order in $CePd_{1-x}Ni_xAl$

Specific-heat measurements for the $CePd_{1-x}Ni_xAl$ samples with $x = 0.0196$, 0.05, 0.102 and 0.131 were performed using a dilution refrigerator in the temperature range 0.03 – 2.5 K. In the temperature window 2–300 K, for the samples with $x = 0.05$ and 0.102, specific-heat measurements were carried out at the IFP, Forschungszentrum Karlsruhe, within PPMS.

The C/T versus T data are presented in Fig. 7.4. The CePdAl compound ($x = 0$) shows a clear λ-type anomaly at the Néel temperature $T_N = 2.7$ K. The anomaly broadens for the doped compounds, and T_N moves towards lower temperatures with increasing Ni content. For the sample with $x = 0.102$ the antiferromagnetic (AF) transition is still visible as a weak shoulder in C/T around 1 K. At $x_c = 0.131$ the AF transition is seen at about 0.25 K in logarithmic scale (see fig. 7.8). This Ni concentration is already very close to QCP.

From the linear fit of the C/T versus T^2 dependence at low temperatures (see Fig. 7.5) the electronic specific-heat coefficients γ have been estimated for the series $CePd_{1-x}Ni_xAl$. Results are summarized in Table 7.1:

γ grows with increasing Ni content, reaching value of 1.3 $JK^{-2}mol^{-1}$ for $x = 0.131$, which indicates enhanced Kondo screening.

Figure 7.6 displays the magnetic contribution to the specific-heat, $C_{\mathrm{mag}} = C_{\mathrm{CePdAl}} - C_{\mathrm{LuPdAl}}$, as a function of the reduced temperature T/T_N. From C_{mag} data the magnetic contribution to the entropy S_{mag} has been calculated (see Fig. 7.7). In all compounds S_{mag} at T_N is lower than $R \ln 2 = 5.76$ $JK^{-1}mol^{-1}$ corresponding to the doublet ground state. Moreover, a deviation from $R \ln 2$ becomes more significant for a larger Ni content: this is the evidence of the enhanced screening of local moments due to the Kondo effect.

From specific-heat measurements, the QCP was estimated at $x_c \approx 0.13$ for $CePd_{1-x}Ni_xAl$ (see Fig. 7.4). The transition temperature at this Ni consentration is essentially suppressed. Previous specific-heat measurements on doped compounds $CePd_{1-x}Ni_xAl$ have shown that a critical Ni concentration is $\sim 10\%$ [61].

x	γ (J/molK^2)
0	0.281
0.020	0.369
0.050	0.641
0.102	1.154
0.131	1.309

Table 7.1: Electronic specific-heat coefficient for $CePd_{1-x}Ni_xAl$.

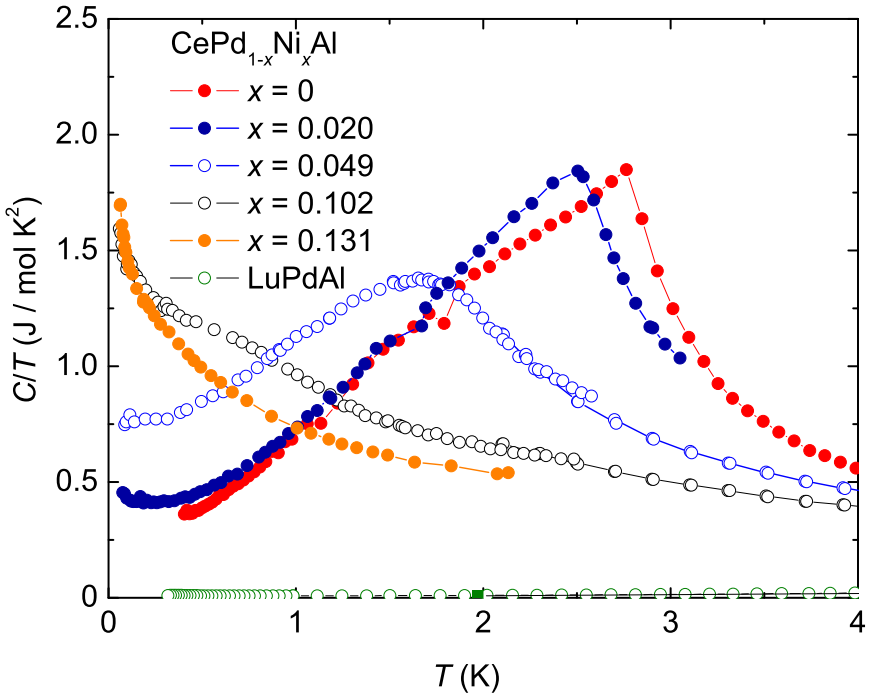

Figure 7.4: C/T versus T for $CePd_{1-x}Ni_xAl$ (x = 0, 0.0196, 0.05, 0.102, 0.131).

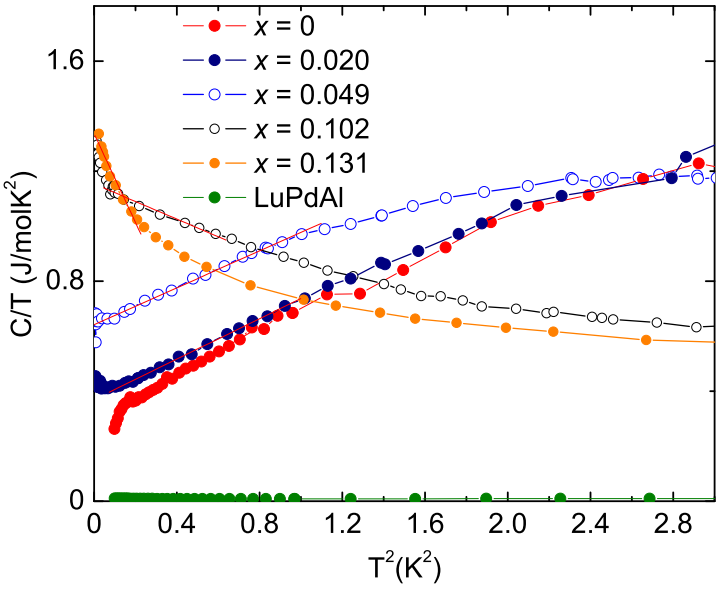

Figure 7.5: C/T versus T^2 for $CePd_{1-x}Ni_xAl$ alloys (x = 0, 0.0196, 0.05, 0.102, 0.131)

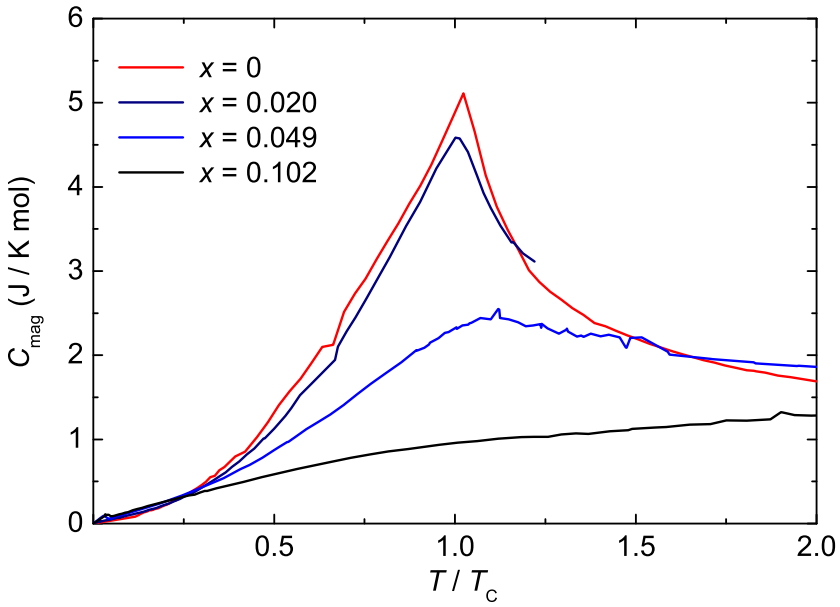

Figure 7.6: Magnetic specific-heat versus T/T_N for $CePd_{1-x}Ni_xAl$ alloys.

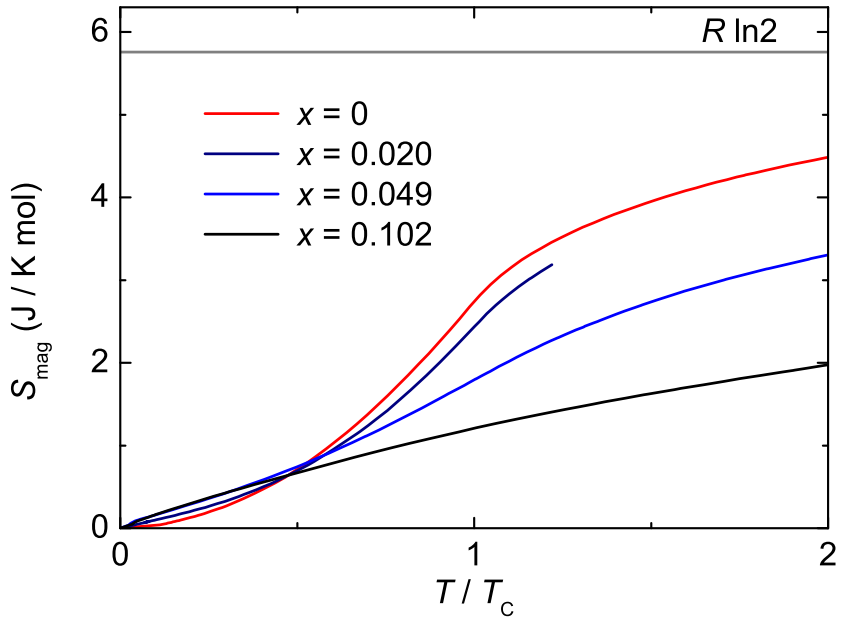

Figure 7.7: Magnetic entropy versus T/T_N for $CePd_{1-x}Ni_xAl$.

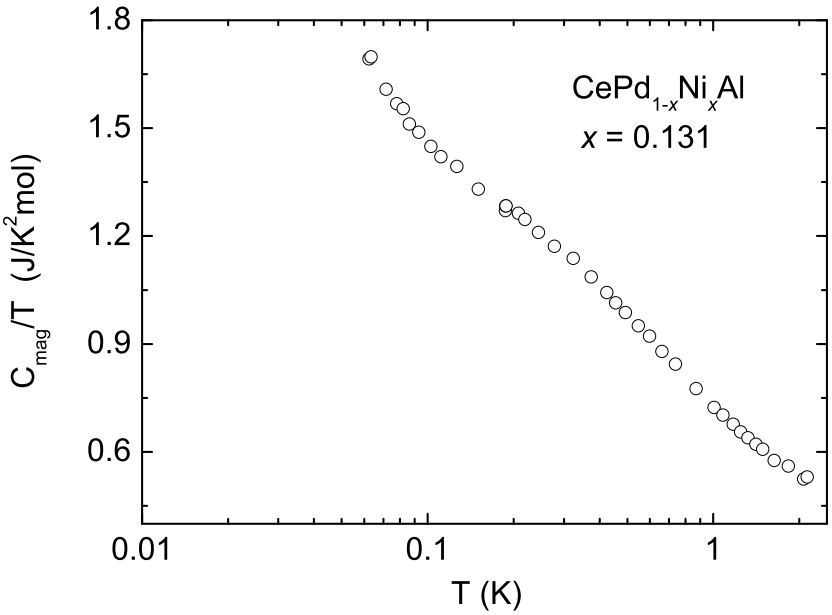

Figure 7.8: Magnetic specific-heat for $CePd_{1-x}Ni_xAl$ ($x = 0.131$) alloy.

7.3 AC-susceptibility

7.3.1 Spin-glass behaviour

In magnetic systems with frustrated bonds superimposed with structural disorder (which can not be excluded in our polycrystalline samples $CePd_{1-x}Ni_xAl$) one may observe a spin-glass-like behaviour in the AC-susceptibility signal $\chi_{AC}(T,\omega)$, which acquires a dependence on the frequency $\omega = 2\pi f$ of the applied magnetic field. In order to explore frustrated interactions, we have performed measurements of $\chi(T,\omega)$ on CePdAl and $CePd_{1-x}Ni_xAl$ samples in the frequency range $200 < \omega/2\pi < 5100$ Hz down to 300 mK.

The results for CePdAl are presented in Fig. 7.9. The AC susceptibility exhibits a maximum ($T_m \approx 2.5$ K $< T_N = 2.7$ K) which shifts to higher temperatures with increasing ω — a behaviour usually observed in spin-glass systems. Our results agree with previous studies of the AC susceptibility in CePdAl [58]. From the set of measurements presented in Fig. 7.9, we have estimated $\Delta T_m/(T_m \Delta \log(f)) \approx 0.12$/decade f (see Fig. 7.10), which is one order of magnitude larger than in conventional spin-glass [59].

Examples of $\chi(T,\omega)$ measurements for the doped $CePd_{1-x}Ni_xAl$ with x = 0.0196 and 0.0899 are presented in Figs. 7.11 and 7.12, respectively, where frequencies of the external field are $f_0 = 5057$ Hz and $f_1 = 217$ Hz. Again, a shift of the maximum T_m in χ_{AC} towards higher temperature is seen for a larger frequency $f_0 > f_1$. Estimation of $\Delta T_m/(T_m \Delta \log f)$ for the doped samples yields the values 0.18/decade f for x= 0.020, 0.11/decade f for x= 0.067, and 0.019/decade f for x= 0.083.

Following Li *et al.* [58], we suggest that the ω-dependence of $\chi_{AC}(T,\omega)$ could originate from the triangular magnetic structure and the existence of structural disorder in the samples.

7.3.2 Doping tuning towards the critical point

In addition to specific-heat studies, the AC susceptibility measurements allow to yield the transition temperature T_N for doped compounds $CePd_{1-x}Ni_xAl$ and explore an approach to a possible QCP.

Measurements of χ_{AC} for the series of samples with x = 0.0, 0.020, 0.067, 0.083 and 0.105 were carried out. Because of the ω-dependence of χ_{AC}, the data for the highest frequency $f_0 = 5057$ Hz has been used to determine the onset of ordering: it supports the value $T_N = 2.7$ K for CePdAl in agreement with literature and specific-heat data. The background signal has been subtracted out and the resulting $\chi_{AC}(T)$ curves

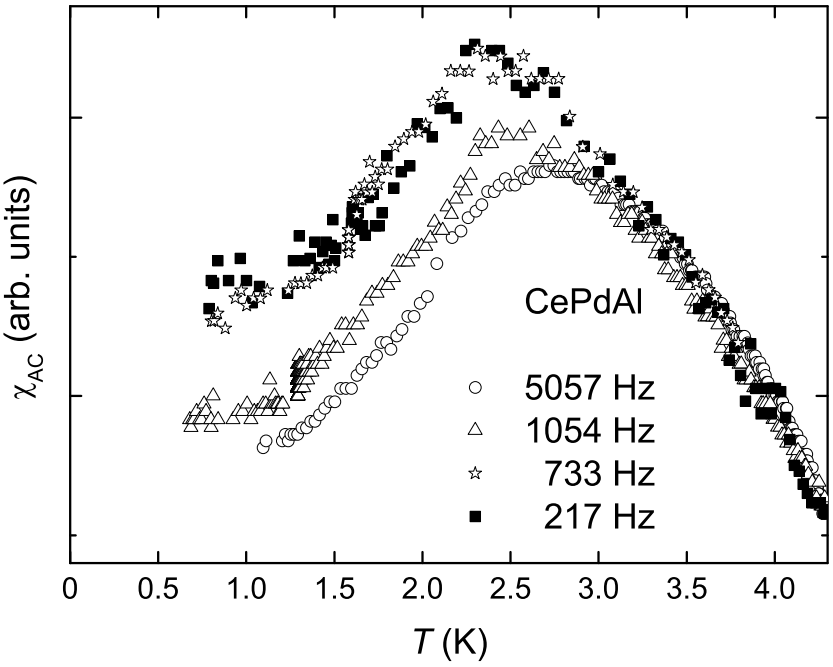

Figure 7.9: AC-susceptibility versus T of CePdAl measured at different frequencies f.

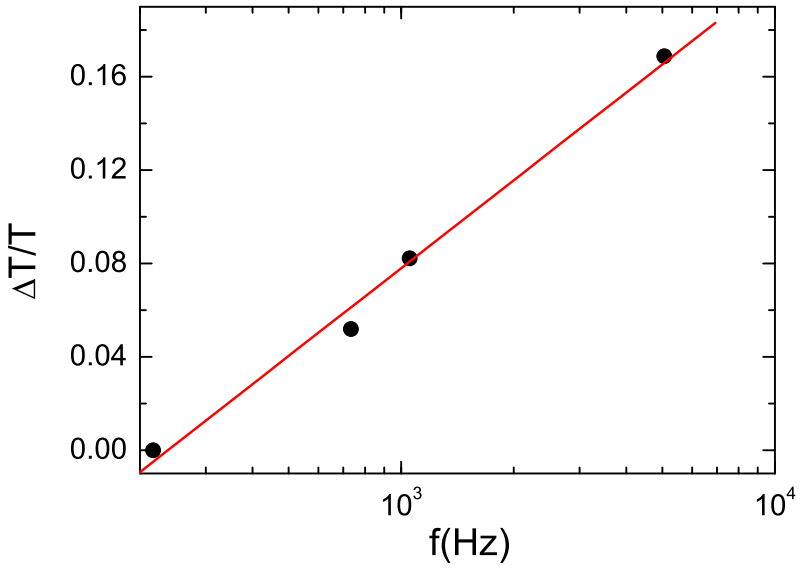

Figure 7.10: $\Delta T_m/T_m$ versus f for CePdAl, where T_m refers to maximum of $\xi_{\mathrm{AC}}(T)$ shown in Fig. 7.9

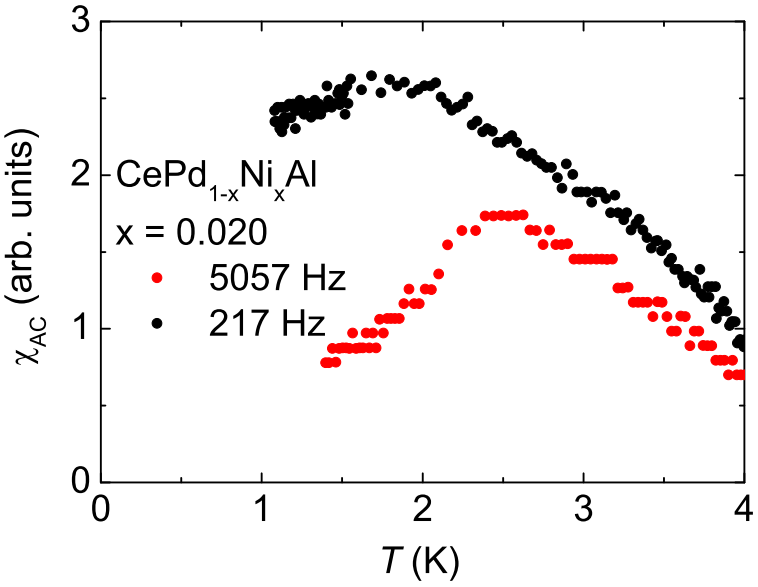

Figure 7.11: AC-susceptibility versus T of $CePd_{1-x}Ni_xAl$ ($x = 0.020$) at different frequencies.

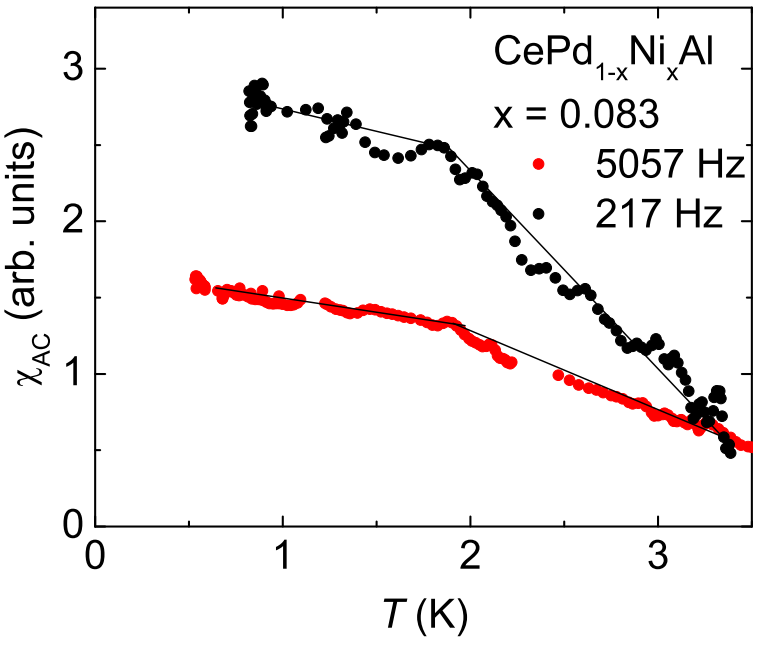

Figure 7.12: AC-susceptibility versus T of $CePd_{1-x}Ni_xAl$ ($x = 0.083$) at different frequencies.

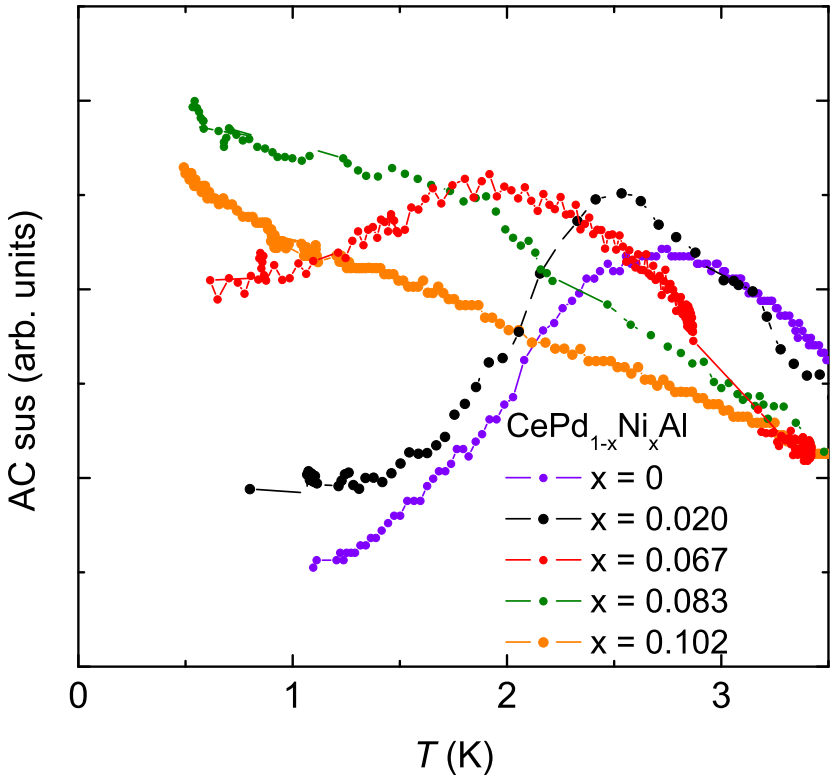

Figure 7.13: AC susceptibility versus T of $CePd_{1-x}Ni_xAl$ at 5057 Hz for different x values.

(see Fig. 7.13) have been scaled according to the individual masses of the samples. We mention that errors may occur (i) from a different filling factor for each of the samples, (ii) from different orientations of the samples inside the pick-up coil, and (iii) from a different shapes of the samples. We have attempted to minimize these effects by mechanical tuning the sample position in the coil. Since errors in the precise definition of mass, in the filling factor and, mainly, in the background signal are unavoidable, all χ_{AC} curves in Fig. 7.13 were shifted in the same point at $T = 4$ K. Therefore, we consider as reliable data only the transition temperatures (which are reproducible in all series of measurements), but not the magnitudes of χ_{AC}.

The χ_{AC} data are presented in Fig. 7.13. A maximum of $\chi_{AC}(T)$ defines the Néel temperature $T_N(x)$, which shifts towards 0 K when the Ni content x is increased. The maximum evolves to a "weak shoulder" when approaching the QCP ($x = 0.083$ and 0.102). In Fig. 7.14 we have summarized the results on $T_N(x)$ obtained both from the specific-heat and the AC susceptibility mea-

surements. The dashed line shows a fit, $T_N(x) = T_N(0)|x - x_c|^{1/2}$, illustrating a critical behaviour of $CePd_{1-x}Ni_xAl$ compounds: when *chemical pressure* is exerted on the system the magnetic order is weakened as expected from a correlation between doping and hydrostatic pressure effects as discussed for Ce(Ni-Pt) compounds in the previous Chapters 4 and 5. In particular, comparing our data on χ_{AC} with that on CePdAl under hydrostatic pressure [54], one may argue that 8.3% Ni doping corresponds to a pressure $\simeq 0.6$ GPa.

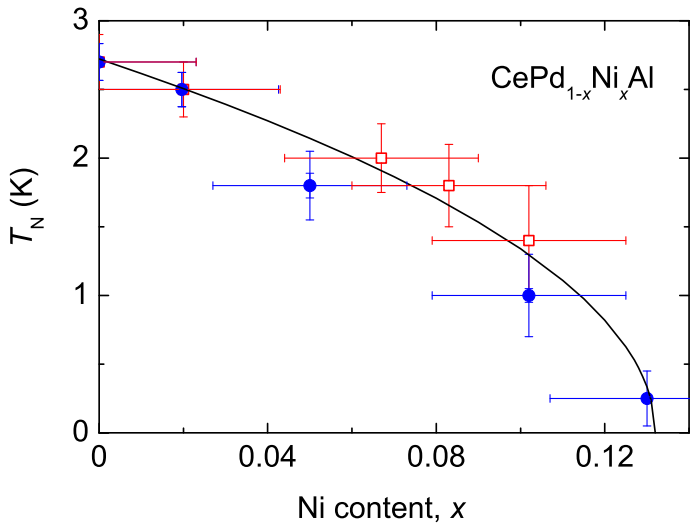

Figure 7.14: Concentration dependence of T_N for doped compounds $CePd_{1-x}Ni_xAl$. Closed circles are results of specific-heat measurements, open squares are obtained from AC susceptibility at f=5057 Hz.

7.4 DC-susceptibility and magnetisation

Effects of disorder in systems with frustrated magnetic interactions can be revealed by examining the DC-susceptibility. We have performed $\chi_{DC}(T)$ measurements on $CePd_{1-x}Ni_xAl$ using the VSM in the magnetic field of 0.1 T, and in the temperature range 2–300 K. Before the measurements, the samples were powdered to avoid undesirable effects of possible textures.

At high temperature, χ_{DC} satisfies the Curie-Weiss law $\chi = C/(T - \Theta)$, the corresponding paramagnetic effective moments μ_{eff} and Weiss-temperatures Θ are presented in Table 7.2. We found μ_{eff} to be slightly smaller than the magnetic moment $2.54\mu_B$ of a free Ce^{3+} ion. The negative Curie-Weiss temperature Θ indicates an antiferromagnetic interaction between magnetic moments. The maxima of χ_{DC} curves (see Fig. 7.15) were used to find the AF transition temperatures T_N (Table 7.2), which were slightly larger than those found from specific-heat measurements.[2] For x=0.0899 and x=0.102 where no maxima were observed, the kinks in $\chi(T)$ were taken as ordering temperature. The ratio Θ/T_N is usually taken to characterize the degree of frustration: it grows (see Table 7.4) with increasing Ni content, indicating the presence of magnetic disorder and an increased amount of frustrated bonds caused by impurity atoms.

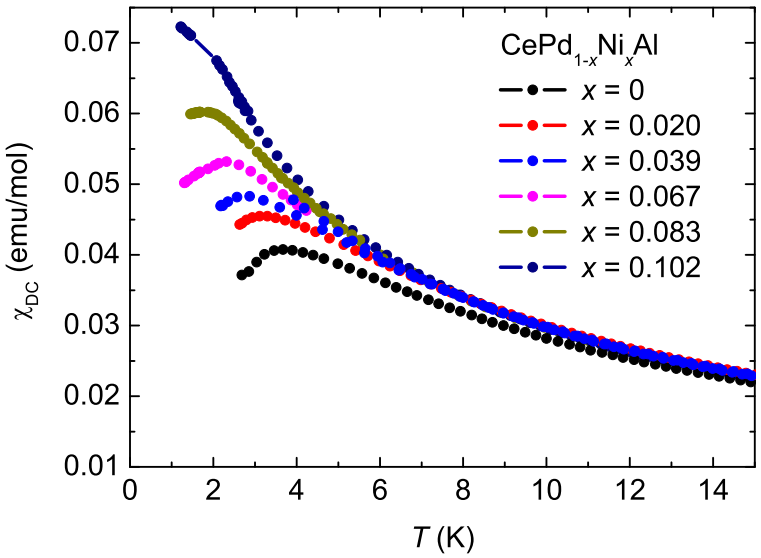

Figure 7.15: DC-susceptibility for $CePd_{1-x}Ni_xAl$ samples in the low temperature range. A suppression of the Néel temperature is seen in a peak which shifts towards 0 K. A larger magnitude of the M/H signal (measured at 0.1 T) at larger x originates from peculiarities of the magnetisation curves at small fields, as shown in Figures 7.16 and 7.17.

[2]Pressure measurements in the magnetic field 0.1 T on CePdAl reported by S. Hane *et al.* [60] revealed an enhanced value of T_N as well.

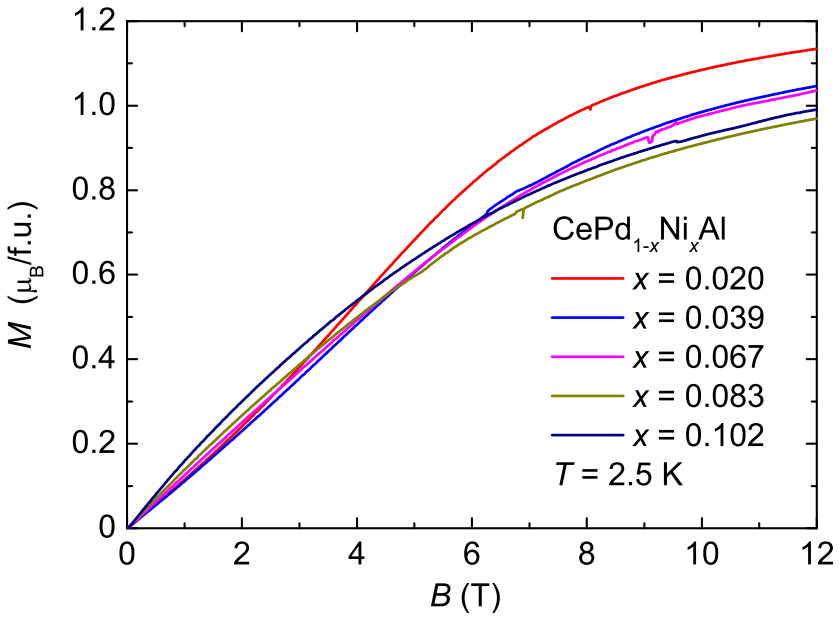

Figure 7.16: Magnetisation of $CePd_{1-x}Ni_xAl$ samples in magnetic field up to 12 T.

x	μ_{eff}/Ce atom (μ_B)	Θ (K)	T_N (χ_{DC}) (K)	T_N (χ_{AC}) (K)	Θ/T_N
0	2.42	−35.7	3.3	2.7	10.8
0.020	2.41	−31.5	3.1	2.5	10.2
0.039	2.42	−32.5	2.6	-	12.5
0.067	2.46	−35.7	2.3	2	15.5
0.083	2.42	−32.4	-	1.8	18
0.102	2.41	−32.2	-	1.4	23

Table 7.2: Effective magnetic moments, Weiss-temperatures and Néel temperatures for powder samples $CePd_{1-x}Ni_xAl$.

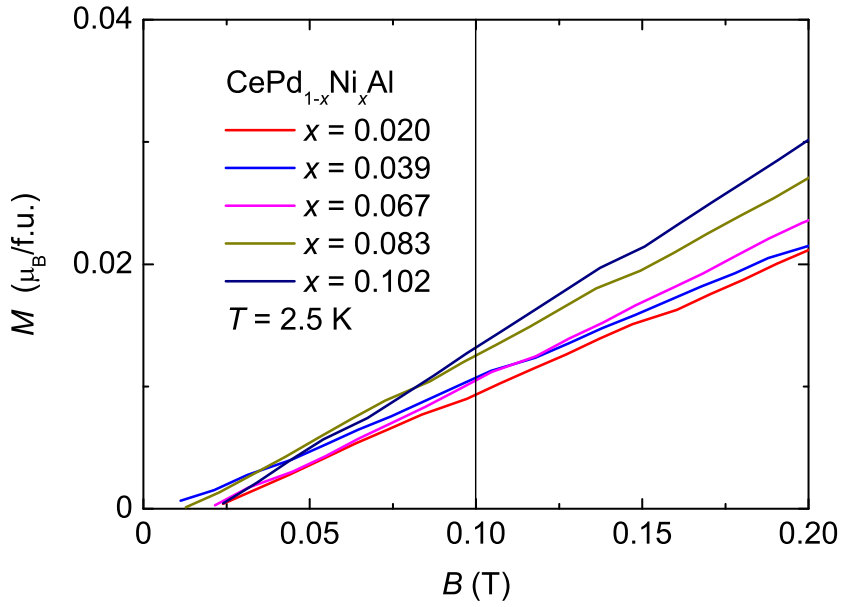

Figure 7.17: Magnetisation of $CePd_{1-x}Ni_xAl$ samples in the low-field region. The value 0.1 T was used for DC-susceptibility measurements to determine χ_{DC} (see Fig.7.15).

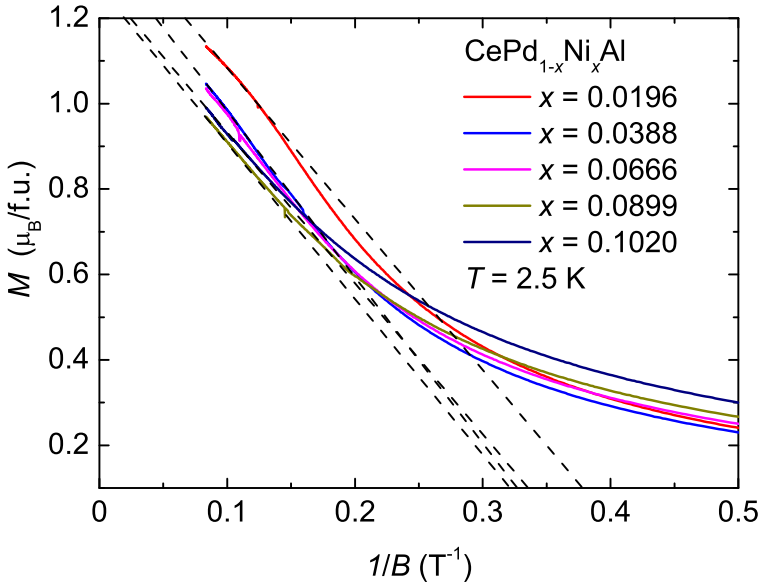

Figure 7.18: Magnetisation of $CePd_{1-x}Ni_xAl$ samples versus inverse magnetic field B^{-1}.

Another evidence of spin-glass-like behaviour in $CePd_{1-x}Ni_xAl$ comes from the low-temperature ($T = 2.5$ K) magnetisation curves shown in Fig. 7.16: here M does not saturate even at high field of 12 T, where the effect is more pronounced for a larger amount of impurity Ni atoms. To make this observation clear, we show M versus B^{-1} in Fig. 7.18. The region $B > 5$ T ($B^{-1} < 0.2$ T^{-1}) can be described by

$$M(B) = M_\infty - \frac{K}{B},$$

where K is a constant. Such an asymptotic behaviour (shown by dashed lines in Fig. 7.18) agrees with a behaviour of typical spin-glasses (see, e.g. [59]).

Appendix

compound	B (exp), GPa	source	B_{VR} (GPa)	B_{Voigt} (GPa)	B_{Reuss} (GPa)
$CeSn_3$	54	[62]	44.9	40.8	49
$CePd_3$	102.5	[63]	102.2	63.4	140.1
$CeBe_{13}$	81.6	[64]	87.1	79.5	94.7
	89	[65]			
CeB_6	168	[64]	121.5	87.3	155.6
$CeCu_2Si_2$	80.5	[66]	79.1	61.1	97.1
	125	[67]			
$CeRu_2Si_2$	105	[68]	99...120.2	65.9...68.5	132...171.8
$CeCu_2Ge_2$	79	[69]	72.8	57.2	88.5
CeAg	50.5	[70]	48	35.4	60.6
CeAl	59.6	[71]	40.2	33.2	47.2
CeNi *			71.3	38.6	104.1
CePt	83.3	[38]	94.9	39.9	149.9

Table A1: Bulk modulus for heavy-fermion compounds compiled by K. Grube [45]. *For CeNi compound no valid experimental data are available.

Summary

The Ce-based heavy-fermion compounds, ferromagnetic $CeNi_xPt_{1-x}$ and antiferromagnetic $CePd_{1-x}Ni_xAl$, investigated in the present work, reveal properties of Kondo systems and exhibit magnetic ordering at low temperatures. By means of doping and applying hydrostatic pressure, these systems were driven towards quantum phase transition. Close to the transition, the non-Fermi-liquid and spin-glass like behaviour was observed.

The effect of doping with Ni atoms of ferromagnetic CePt was widely studied in the literature. A dependence of the transition temperature on the impurity concentration resembles the Doniach diagram, reflecting the competition between Kondo screening and the RKKY interaction. The $CeNi_xPt_{1-x}$ alloys reveal the properties of intermediate valence compounds at $x > 0.9$. However, prior to this work it was not clear whether the system undergoes a quantum phase transition, i.e. magnetic transition at T=0. We have investigated the effect of hydrostatic pressure on compounds with $x = 0.85$ and $x = 0.9$. At ambient pressure, they are close to the quantum critical point but are ordered ferromagnetically below 6.2 and 4 K, respectively. From measurements of the temperature and magnetic-field dependences of the sample magnetisation we can conclude that magnetic order in both studied compounds is suppressed by hydrostatic pressure. The Curie temperatures at different pressures have been found using the Arrott plot method. An estimation of the critical pressure for both compounds is performed yielding $p_c \approx 0.95$ GPa for $CeNi_{0.9}Pt_{0.1}$, and $p_c \approx 1.3$ GPa for $CeNi_{0.85}Pt_{0.15}$.

Comparing the crystal cell compression by Ni doping and by hydrostatic pressure, we show that for the $CeNi_xPt_{1-x}$ system close to the quantum critical point, hydrostatic pressure suppresses the Curie temperature T_C towards zero faster as compared to Ni doping with the same volume. Therefore, by doping CePt with Ni atoms, being isovalent to Pt, the effect of electronic structure modification plays a significant role close to the quantum phase transition.

The antiferromagnetic CePdAl has $T_N = 2.7$ K. Its magnetic structure can be mapped on a Kagomé-like lattice with frustrated bonds. The effect of

hydrostatic pressure on magnetic ordering was investigated in the literature, yielding T_N=0 for a critical pressure 0.95 GPa. Previous specific-heat measurements on doped compounds $CePd_{1-x}Ni_xAl$ have shown that a critical Ni concentration is $\sim 10\%$, in our work, the effect of chemical pressure has been investigated systematically. The changes in the specific heat, magnetisation, and AC susceptibility are studied in detail for a Ni concentration ranging from 0 up to $x_c = 0.13$. The critical concentration is estimated as $x_c \approx 0.13$, where system undergoes a quantum phase transition. At $x_c = 0.13$ T_N is essentially suppressed.

The AC susceptibility of doped compounds $CePd_{1-x}Ni_xAl$ shows a spin-glass like behaviour. This indicates the presence of magnetic disorder and increased amount of frustrated bonds due to impurity atoms.

Further investigations should be performed on single crystalline samples of $CePd_{1-x}Ni_xAl$. The susceptibility measurements at different frequencies may clarify the origin of the spin-glass behaviour observed in this work. Moreover, it would be interesting to measure the specific heat on a CePdAl single crystal at different magnetic fields along different crystallographic directions. That is because magnetic field is an external parameter which can alter the spin ordering in the system.

Bibliography

[1] A. A. Abrikosov, L. P. Gor'kov, and I. E. Dzyaloshinskii, *Quantum field theoretical methods in statistical physics.* Oxford, New York, Pergamon Press (1965).

[2] L. Kantorovich, *Quantum theory of the solid state: an introduction*, Kluwer Academic Publishers (2004).

[3] H. v. Löhneysen, A. Rosch, M. Vojta, and P. Wölfle, Rev. Mod. Phys. **79**, 1015 (2007).

[4] C. Petrovic, R. Movshovich, M. Jaime, P. G. Pagliuso, M. F. Hundley, J. L. Sarrao, Z. Fisk, and J. D. Thompson, Europhys. Lett., **53**, 354 (2001).

[5] G. R. Stewart, Z. Fisk, and M. S. Wire, Phys. Rev. B, **30**, 482 (1984).

[6] A. Bianchi, R. Movshovich, I. Vekhter, P. G. Pagliuso, and J. L. Sarrao, Phys. Rev. Lett. **91**, 257001 (2003).

[7] Robert M. White, *Quantum Theory of Magnetism*, 3rd Edition, Springer-Verlag (2007).

[8] H. v. Löhneysen, Hyperfine Interactions **104**, 127 (1997).

[9] D. W. Hess, P. S. Riseborough, and J. L. Smith, *Heavy-fermion phenomena.* Encyclopedia of Applied Physics, **7**, 435 (1993).

[10] T. Görlach, *Tieftemperatureigenschaften der intermetallischen Ce-und Yb-Verbindungen* $CePtAl_3$, $La_{1-x}Ce_xCu_6$ *und* $YbPd_{1-x}Pt_xSn$. Doktorarbeit, Universität Karlsruhe (2006).

[11] K. G. Wilson, Rev. Mod. Phys. **47**, 773 (1975).

[12] J. M. Robinson, Phys. Rep. **51**, 1 (1979).

[13] J. H. Jefferson and W. H. Stevens, J. Phys. C **9**, 2151 (1976).

[14] P. W. Anderson, Phys. Rev. **124**, 41 (1961).

[15] J. Kondo, Prog. in Theor. Phys. **32**, 37 (1964).

[16] B. Cornut, B. Coqblin, Phys. Rev. B **5**, 4541 (1972).

[17] S. Doniach, Physica B **91**, 231 (1977).

[18] J. A. Hertz, Phys. Rev. B **14**, 1165 (1976).

[19] A. J. Millis, Phys. Rev. B **48**, 7183 (1993).

[20] G. R. Stewart, Rev. Mod. Phys. **73**, 797 (2001).

[21] Q. Si, S. Rabello, K. Ingesent, and J. L. Smith, Phys. Rev. B **68**, 115103 (2003).

[22] P. Coleman, Physika B **259-261**, 353 (1999).

[23] R. Allmann, *Röntgen-Pulverdiffraktometrie*, Springer (2002).

[24] A. Kent, *Experimental low-temperature physics*, Macmillan Physical Science Series, AIP Press (1993).

[25] S. Foner Rev. Sci. Instr. **30**, 548 (1959).

[26] G.–F. von Blanckenhagen and G. R. Stewart, Solid State Comm. **108**, 535 (1998).

[27] D. Gignoux, J. C. Gomez-Sal, J. Appl. Phys. **57**, 3125 (1985).

[28] D. Gignoux, and J. C. Gomez-Sal, Solid State Commun. **45**, 779 (1983).

[29] D. Gignoux, F. Givord, R. Lemaire, and F. Tasset, J. Magn. Magn. Matter **50**, 53 (1985).

[30] J. I. Espeso, J. C. Gomez Sal, J. Chaboy, Phys. Rev. B **63**, 014416 (2000).

[31] D. Gignoux, J. C. Gomez-Sal, Phys. Rev. B **30**, 3967 (1984).

[32] A. K. Grover, L. C. Gupta, and R. Vijayaraghavan, Physica B **86-88**, 81 (1977).

[33] H. Lueken, M. Meier, G. Klessen, and W. Bruder, J. Less Common Metals. **63**, 35 (1979).

[34] A. Schröder, R. van den Berg, H. v. Löhneysen, W. Paul, H. Lu, Solid State Communications, **65**, 99 (1988).

[35] R. R. Josef, K. A. Gschneidner, and R. E. Hungsberg, Phys. Rev. B **5**, 1878 (1972).

[36] H. Gamari-Seal, J. Less Common Metals **75**, 43 (1980).

[37] J. Larrea, M. B. Fontes, A. D. Alvarenga, E. M. Baggio-Saitovitch, T. Burghardt, and A. Eichler, M. A. Continentino, Phys. Rev. B **72**, 035129 (2005).

[38] Y. Itoh, H. Kadomatsu, M. Kurisu, and H. Fujiwara, J. Phys. Soc. Jpn. **56**, 1159 (1987).

[39] D. Gignoux, F. Givord, R. Lemaire, F. Tasset, J. Phys. **43**, C7, 257 (1982).

[40] D. Gignoux and J. Voiron, Phys. Let. **108**, 473 (1985).

[41] A. Arrott, Phys. Rev. **108**, 1394 (1957).

[42] I. Yeung, R.M. Roshko, and G. Williams Phys. Rev. B **34**, 3456 (1986).

[43] S. V. Tyablikov, *Methods in the quantum theory of magnetism.* New York, Plenum (1967).

[44] Ch. Kittel, *Thermophysical properties of materials.* Amsterdam, Lausanne, New York, Oxford, Shannon, Singapore, Tokyo, Elsevier (1999).

[45] K. Grube, private communication (2008).

[46] Ch. Kittel, *Einfürung in die Festkörperphysik. 13. Auflage.* München, Wien, Oldenbourg (2002).

[47] A. Oyamada, K. Kamioka, K. Hashi, S. Maegawa, T. Goto, H. Kitazawa, J. Phys. Soc. Jpn. **65**, Suppl. B, 128 (1996).

[48] Y. Isikawa, T. Mizushima, N. Fukushima, T. Kuwai, J. Sakurai, and H. Kitazawa, J. Phys. Soc. Jpn. **65**, Suppl. B, 117 (1996).

[49] A. Dönni, G. Ehlers, H. Maletta, P. Fischer, H. Kitazawa, and M. Zolliker, J. Phys.: Condens. Matter **8**, 11213 (1996), and references therein.

[50] M. Dolores Núñes-Regueiro, C. Lacroix, and B. Canals, Physica C **282-287**, 1885 (1997).

[51] A. Oyamada, S. Maegawa, M. Nishiyama, H. Kitazawa, and Y. Isikawa, Phys. Rev. B **77**, 064432 (2008).

[52] J. Tang, A. Matsushita, H. Kitazawa, and T. Matsumoto, Physica B **217**, 97 (1996).

[53] S. Akamaru, Y. Isikawa, T. Kuwaia, T. Mizushimaa, J. Sakuraia and Y. Uwatoko, Physica B **312-313**, 466 (2002).

[54] T. Goto, S. Hane, K. Umeo, T. Takabatake, and Y. Isikawa, Chem. of Solids, **63**, 1159 (2002).

[55] R. Burriel, M. Castro, J. A. Blanco, J. I. Espeso, J. Rodríguez Fernández, J. C. Gómez-Sal, C. Lester, M. de Podesta, and K. A. McEwen, Physica B **206-207**, 264 (1995).

[56] J. A. Blanco, M. de Podesta, J. I. Espeso, J. C. Gómez-Sal, C. Lester, K. A. McEwen, N. Patrikos, and J. Rodríguez Fernández, Phys. Rev. B **49**, 15126 (1994).

[57] H. M. Rosenberg, *Low temperature solid state physics*. Oxford University Press (1965).

[58] D. X. Li, S. Nimori, H. Kitazawa, and Y. Shiokawa, Physica B **378-380**, 805 (2006).

[59] J.A. Mydosh, *Spin glasses: An experimental introduction.* Taylor & Francis, London (1993).

[60] S. Hane, T. Goto, T. Abe, and Y. Isikawa., Physica B **281–282**, 391 (2000).

[61] Y. Isikawa, T. Kuwai, T. Mizushima, T. Abe, G. Nakamura, and J. Sakurai, Physica B **281 - 282**, 365 (2000).

[62] R. Takke, M. Niksch, W. Assmus, B. Lüthi, R. Pott, R. Schefzyk, and D. K. Wohlleben, Z. Phys. B **44**, 33 (1981).

[63] R. Takke, and W. Assmus, J. Crystal Growth **49** 97 (1980).

[64] B. Lüthi, J. Magn. Magn. Mater **52**, 70 (1985).

[65] J. M. Leger, and A. M. Redon J. Less-Common Met. **156**, 137 (1989).

[66] A. P. G. Kutty, and S. N. Vaidya, in Theoretical and Experimental Aspect of Valence Fluctuations and Heavy Fermions, edited by L. C. Gupta and S. K. Malik 621(Plenum, New York, 1987).

[67] R. Mock, B. Hillebrands, H. Schimidt, G. Gntherodt, Z. Fisk, and A. Meyer, J. Magn. Magn. Mater. **47-48**, 312 (1985).

[68] A. Lacerda, A. de Visser, P. Haen, P. Lejay, and J. Flouquet, Phys. Rev. B. **40**, 8759 (1989).

[69] C. Wassilew-Reul, M. Kunz, M. Hanfland, D. Häusermann, C. Geibel, and F. Steglich, Physica B **230-232**, 137 (1997).

[70] R. Takke, N. Dolezal, W. Assmus, and B. Lthi, J. Magn. Mater. **23**, 247 (1981).

[71] R. Takke, M. Niksch, W. Assmus and B. Lthi, R. Pott,R. Schefzyk, and D. K. Wohlleben, Z. Phys. B **44**, 33 (1981).

Acknowledgments

I would like to express my gratitude to Prof. Dr. H. von Löhneysen for giving me a possibility to perform a PhD work in his group, for the interesting research topic and support during all the years spent in Karlsruhe.

I would like to thank Prof. Dr. E. Dormann for second refereeing of this PhD thesis.

Thanks to my supervisor Dr. V. Fritsch for her advices, constant support and fruitful discussions.

I am extremely grateful to Prof. Dr. G. Goll, Prof. Dr. B. Pilawa, Dr. M. Uhlarz, Dr. C. Sürgers, Dr. S. Drobnik, Dr. K. Grube, Dr. P. Adelmann, Dr. T. Wolf, K. Hugle for their help in different measurements and interpretation of data.

I would like to thank all my colleagues in Physikalisches Institut, especially S. Drotziger, M. Marz, R. Montbrun, M. Müller, T. Tomanic, D. Stöffler, for a friendly atmosphere and a team work.

I am thankful to Feinmechanischen Werkstatt led by R. Dehm, and Elektronik-Werkstatt for technical support, as well to L. Behrens for his enormous help with computer related issues.

My special thanks belong to my own family for the unprecedented patience and support during the last years spent in doing this work.